Spring 5-2015

# Optical Bistability with Two Serially Integrated InP-SOAs on a Chip

Michael Edward Plascak
*Rose-Hulman Institute of Technology*

**Optical Bistability with Two Serially Integrated InP-SOAs on a Chip**

A Thesis

Submitted to the Faculty

of

Rose-Hulman Institute of Technology

By

Michael Edward Plascak

In Partial Fulfillment of the Requirements for the Degree

Of

Master of Science in Optical Engineering

May 2015

**ROSE-HULMAN INSTITUTE OF TECHNOLOGY**

**Final Examination Report**

Michael E. Plascak — Name

Optical Engineering — Graduate Major

Thesis Title: Optical Bistibility with Two Serially Integrated INP-SOAs on a Chip

**DATE OF EXAM:** May 11, 2015

**EXAMINATION COMMITTEE:**

| | Thesis Advisory Committee | Department |
|---|---|---|
| Thesis Advisor: | Azad Siahmakoun | PHOE |
| | Sergio Granieri | PHOE |
| | Bruce Black | ECE |
| | | |
| | | |

**PASSED** X **FAILED** _____

# ABSTRACT

Plascak, Michael Edward
M.S.O.E.
Rose-Hulman Institute of Technology
May 2015
Optical Bistability with Two Serially Integrated InP-SOAs on a Chip
Thesis Advisor: Dr. Azad Siahmakoun

A photonic switch using two series-connected, reverse-biased semiconductor optical amplifiers integrated onto a single device has been proposed and switching operation has been verified experimentally. The switching operates on two principles; an electrical bistability arising from the connection of two p-i-n structures in series, and the quantum confined Stark effect in reverse-biased multiple quantum well structures. The result is an electroabsorption modulation of the light through the SOAs due to the alternating voltage states. The system simultaneously produces outputs with both inverted and non-inverted hysteresis behavior, with experimental switching speeds demonstrated up to 400 kHz for a reverse-bias voltage of $V_{RB}$=2.000V.

## DEDICATION

I dedicate this thesis to Stephanie. Thank you for your loving support and for helping me through the tough times.

## ACKNOWLEDGEMENTS

I would like to acknowledge all of the Rose-Hulman faculty and staff, and my fellow PHOE students, who have all helped me in my time at this great school. Without their knowledge, guidance, and assistance I could not have achieved the things that I have today. Specifically, I would like to thank:

Dr. Azad Siahmakoun, thank you for affording me a chance to return to Rose-Hulman and pursue a graduate education and research in optics, and for always believing in me.

Dr. Robert Bunch, thank you for the years of keen advice and guidance, both academic and professional.

Dr. Sergio Granieri, thank you for always being there to help and for encouraging me to pursue graduate education in optics in the first place. I guess you were right all along.

Dr. Charles Joenathan, thank you for all of your assistance through the years, and for helping me return to Rose-Hulman to continue my education in optics.

Dr. Paul Leisher, thank you for your help and advice through the years. You also strongly encouraged me to pursue a graduate education in the first place. I should have listened.

Pam Hamilton, thank for all of your helpful advice through the years, and for always making sure that I was on top of things.

Ben Webster, thank you for all of your help and for making my GA work hours much more enjoyable.

Roger Sladek, thank you for all of your help and insight on the projects and designs that I have worked on through the years. Your work has helped make my life easier countless times.

Sanaz Faryadras, thank you for making the hours working in the lab more fun, and for helping me stay positive.

Perhaps most importantly, I would like to thank my family and friends for their loving support through all of life's journeys.

# TABLE OF CONTENTS

## Contents

**LIST OF FIGURES** ..... iii

**LIST OF TABLES** ..... vi

**LIST OF ABBREVIATIONS** ..... vii

**1. INTRODUCTION** ..... 1

**1.1 Introduction to Switching, Bistability, and Hysteresis Behavior** ..... 2

**2. THEORY** ..... 4

**2.1 Quantum Wells and MQW Structures** ..... 4

**2.2 The Quantum Confined Stark Effect** ..... 7

**2.3 The Self-Electro-Optic Effect Device and Symmetric SEED** ..... 8

**2.4 Symmetric SOA Device Operation: Exploiting QCSE to Achieve Optical Switching** ..... 12

**3. DEVICE STRUCTURE AND PREPARATION** ..... 17

**3.1 Device Structure** ..... 17

**3.2 Device Preparation: Heat Sink and Wire Bonding** ..... 20

**3.3 Impedance Measurements** ..... 24

**3.4 Optical Fiber Alignment System and Electrical Probing** ..... 26

**3.5 Coupling Power Loss** ..... 30

**3.6 Method for Alignment of Optical Fibers for Maximum Power Coupling** ..... 37

**4. EXPERIMENT SETUP, PROCEDURES, AND RESULTS** ..... 40

**4.1 Device Impedance Measurements** ..... 40

**4.2 Characterizing Device Transmission: QCSE** ..... 41

**4.3 Analyzing Bistability at Low Speeds** ..... 44

**4.4 Bistable Switching at Higher Speeds** ..... 51

**4.5 Analysis of System Limitations** ..... 58

**5. CONCLUSIONS AND FUTURE WORK** ..... 68

**LIST OF REFERENCES** ..... 70

**Appendix A: SOA Transmission Measurements for QCSE** ..... 74

# LIST OF FIGURES

Figure Page

Figure 1.1: Diagram showing the behavior of an optically bistable system ..... 3
Figure 2.1: Schematic of a MQW structure with electric field applied perpendicular to the layers, in the direction of confinement. ..... 6
Figure 2.2: Energy band diagram showing the effect of an applied electric field on the quantum well. Notice that the bandgap energy to decrease ($\boldsymbol{h\nu 1 < h\nu 2}$), and the wavefunctions to shift to opposite sides of the well [4]. ..... 7
Figure 2.3: Diagram of the SEED, a device first proposed to produce optical bistability.. 8
Figure 2.4: Schematic of the S-SEED..... 10
Figure 2.5: Schematic of the Symmetric SOA Device ..... 12
Figure 2.6: Load lines demonstrating the electrical bistability of the symmetrically coupled SOA device a) when the power into SOA1 is increasing, and b) when the power into SOA1 is decreasing..... 14
Figure 3.1: Microscope image of the coupled SOA device ..... 18
Figure 3.2: Annotated side-view diagram of coupled SOA device ..... 18
Figure 3.3: Diagram showing the structure of the waveguide and MQW in the SOA ..... 19
Figure 3.4: Picture of coupled SOA device successfully mounted to heat sink ..... 20
Figure 3.5: Picture of K&S manual wire bonder used in wire bonding coupled SOA device to heat sink contact ..... 21
Figure 3.6: Microscope picture of the coupled SOA device being held under the wire bonder with the clamp..... 22
Figure 3.7: Illustration of ball bonding process ..... 23
Figure 3.8: Equivalent circuit model used in measuring diode capacitance..... 25
Figure 3.9: Impedance measurements from Garmy EChem Analyst software ..... 25
Figure 3.10: Top-down schematic of all probes and fibers necessary to observe switching operation ..... 26
Figure 3.11: Annotated picture of fiber alignment and voltage probing setup..... 28
Figure 3.12: Types of waveguide misalignment..... 29
Figure 3.13: (a) 3D electric field profile of a Gaussian beam in a single-mode fiber. (b) Cross-section of the Gaussian profile illustrating parameters $\boldsymbol{\omega 0}$ and the MFD..... 32
Figure 3.14: (a) 3D electric field profile of the fundamental mode in the SOA waveguide. (b) Contour plot of electric field profile. ..... 33
Figure 3.15: Mode cross sections for both directions in the SOA waveguide and in the optical fiber. ..... 34
Figure 3.16: Image of optical fibers aligned with coupled SOA device, all measurements ±5.32μm. Both SOAS measured to same dimensions within uncertainty. ..... 37
Figure 3.17: Diagram showing probe orientation and setup of optical fiber alignment method..... 39

Figure 4.1: Diagram of equipment setup for characterizing spectral transmission ..... 42
Figure 4.2: Spectral T(V) measurements for SOA2 ..... 43
Figure 4.3: Equipment setup for bistable switching at 1kHz modulation frequency..... 45
Figure 4.4: 1kHz sinusoidal optical signal out of the EOM ..... 46
Figure 4.5: Switching voltage signal V (signal 2) along with voltage signal input to modulator (signal 1), system operating at 1kHz frequency ..... 48
Figure 4.6: XY plot of input/output signal to the system, showing bistable switching behavior, system operating at 1kHz frequency..... 48
Figure 4.7: Switching voltage signal across SOA1 (signal 2), plotted along with the voltage input to the EOM (signal 1), system operating at 1kHz frequency..... 50
Figure 4.8: XY Plot of the input/output signals of the system, showing bistable, inverted hysteresis behavior, system operating at 1kHz frequency ..... 50
Figure 4.9: Equipment setup for bistable switching frequencies beyond 1 kHz ..... 52
Figure 4.10: 30 kHz switching voltage V (2), along with the voltage signal into EOM (1) ..... 53
Figure 4.11: XY plot of the input/output of the system operating at 30 kHz switching speed, showing inverted hysteresis behavior ..... 53
Figure 4.12: 100 kHz switching voltage V (2), along with the voltage signal into EOM (1)..... 54
Figure 4.13: XY plot of the input/output of the system operating at 100 kHz switching speed, showing inverted hysteresis behavior ..... 54
Figure 4.14: 200 kHz switching voltage V (2), along with the voltage signal into EOM (1)..... 55
Figure 4.15: XY plot of the input/output of the system operating at 200 kHz switching speed, showing inverted hysteresis behavior ..... 55
Figure 4.16: 300 kHz switching voltage V (2), along with the voltage signal into EOM (1)..... 56
Figure 4.17: XY plot of the input/output of the system operating at 200 kHz switching speed, showing inverted hysteresis behavior ..... 56
Figure 4.18: 400 kHz switching voltage V (2), along with the voltage signal into EOM (1). At this frequency, the voltage signal is much more rounded on the edges than at lower frequencies, looking almost like a sinusoidal signal..... 57
Figure 4.19: XY plot of the input/output of the system operating at 400 kHz switching speed, showing inverted hysteresis behavior ..... 57
Figure 4.20: Diagram showing the effect of tapering a single-mode fiber..... 60
Figure 4.21: Microscope image of a tapered optical fiber used in a commercially available Covega SOA ..... 60
Figure 4.22: Image of tapered optical fibers aligned with SOAs ..... 61
Figure 4.23: Mode cross-sections for both directions in the rectangular waveguide and in optical fiber with a MFD of 2.5μm ..... 63
Figure 4.24: Mode overlap cross-sections showing misalignment for a) coupling from a bare single-mode fiber and b) coupling from a tapered fiber ..... 65

Figure 4.25: Power coupling loss for single-mode and tapered fibers, plotted as a function of lateral misalignmet distance ..... 65
Figure 4.26: Microscope image of the fiber alignment system inside of a commercially packaged SOA ..... 66
Figure 4.27: Tapered optical fibers aligned with the SOA device, showing the length of fiber suspended in air that is necessary to accommodate the tapered fibers in this system ..... 67

# LIST OF TABLES

Table Page

Table 4.1: Input optical power at each wavelength for testing SOA transmission.....43

Table 4.2: System operation parameters for 1 kHz operation when $V_{RB} = 2V$.....48

Table 4.3: System operation parameters for 400 kHz switching operation when $V_{RB} = 2.000V$.....59

Table A.1: Transmission data collected for different bias voltages at λ = 1530nm.....75

Table A.2: Transmission data collected for different bias voltages at λ = 1535nm.....75

Table A.3: Transmission data collected for different bias voltages at λ = 1540nm.....76

Table A.4: Transmission data collected for different bias voltages at λ = 1545nm.....76

Table A.5: Transmission data collected for different bias voltages at λ = 1550nm.....77

Table A.6: Transmission data collected for different bias voltages at λ = 1555nm.....77

Table A.7: Transmission data collected for different bias voltages at λ = 1560nm.....78

# LIST OF ABBREVIATIONS

| | |
|---|---|
| **CW** | Constant Wave |
| **EDFA** | Erbium Doped Fiber Amplifier |
| **EOM** | Electro-Optic Modulator |
| **MBE** | Molecular Beam Epitaxy |
| **MFD** | Mode Field Diameter |
| **MQW** | Multiple Quantum Well |
| **OSA** | Optical Spectrum Analyzer |
| **PC** | Polarization Controller |
| **QW** | Quantum Well |
| **SEED** | Self Electro-optic Effect Device |
| **S-SEED** | Symmetrical SEED |
| **SOA** | Semiconductor Optical Amplifier |

# 1. INTRODUCTION

Fast optical switches are quickly becoming essential components in many advanced photonic systems, including systems for optical computing, optical signal processing, analog to digital conversion, and other applications. One component of particular interest for use as an optical switch is the semiconductor optical amplifier (SOA). Use of SOAs for high bitrate, broadband optical switching in wavelength division multiplexing (WDM) applications has been well documented in the past [1, 2], and continue to be of interest today. SOAs are advantageous in switching applications due to their particularly small footprint, relative simplicity of fabrication (they can be included in integrated photonic devices), and their promise for high data rates. Recent SOA switching architectures have been demonstrated to operate with speeds in excess of 10 Gbits/s [3].

This thesis presents the preparation, system architecture, and operation of a photonic switch using two electrically series-connected, reverse-biased SOAs integrated onto a single, small device. The remainder of Chapter 1 will provide an introduction to switching, optical bistability, and hysteresis behavior in switches. The theoretical background for the coupled SOA device's operation is built in Chapter 2, including a discussion of the quantum confined Stark effect (QCSE) in multiple quantum well (MQW) structures, the use of self electro-optic effect devices (SEEDs) to create optical bistability to achieve switching of optical signals, and an explanation of how it is exploited in this project to create a bistable optical switch. Chapter 3 will serve as an introduction to the symmetrically coupled SOA device itself, as well as device preparation and alignment/voltage probing system architecture. This includes wire-bonding the device, and an overview of the optical alignment, associated losses, and electrical probing system. Chapter 4

contains equipment setup and procedures, along with system operation and device characteristics. Conclusions are drawn in Chapter 5, along with recommendations for improvements and suggestions for possible future research opportunities.

### 1.1 Introduction to Switching, Bistability, and Hysteresis Behavior

In digital communication systems, whether electrical, optical, or otherwise, switching is the process by which signals are selectively directed to different communication channels. Switches are also commonly used in communications to create ones and zeros by changing the signal's level between two states. Such a switch is described as bistable, since the output of the system has two distinct equilibrium states, a high output and a low output. In the instance of an optical bistable switch, the signal level that is being changed is the intensity of the light; if the intensity is below a certain threshold, in the low state, the signal will be registered as a "zero". Conversely, if the intensity of the signal is measured above this threshold – in the high output state – it will be registered as a "one".

A system is truly bistable if it has two output states, $P_{out}$, for the same input level, $P_{in}$. In this case, knowing only the input level $P_{in}$, the output of the system cannot be predicted without more information, since the system's output should depend not only on its current input value, but also on the previous input values. Consider the input/output relationship for an optically bistable system, illustrated in Fig. 1.1. First, notice that there are two "stable" states; when the optical power is sufficiently increased to a certain level, the output will reach an equilibrium to an upper stable state. Conversely, when the optical power is sufficiently low, the output of the system will collapse to a lower stable state. However, notice what happens in between these input power thresholds. For an optical input power of $P_{in1}$ in this region, there are two possible

outcomes, $P_{out1}$ or $P_{out2}$. For an input of $P_{in1}$, the system output power will be $P_{out1}$ only if the signal's power is increasing from the low stable state; additionally, the system output power will be $P_{out2}$ only if the signal's power is decreasing from the upper stable state. The arrows on the curve in the diagram denote the direction in which the input/output relation is moving.

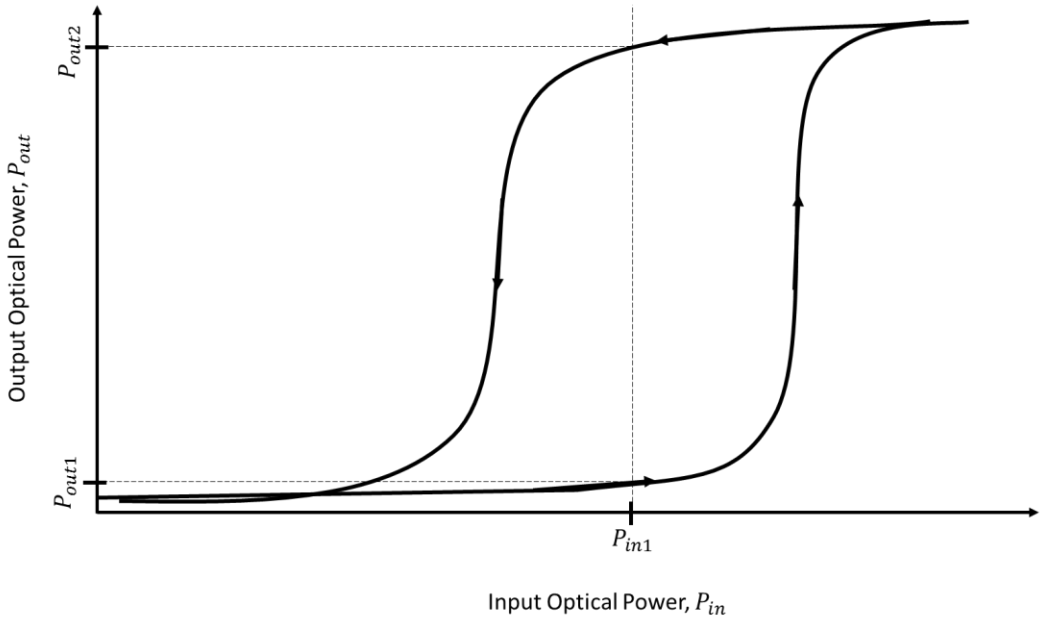


**Figure 1.1: Diagram showing the behavior of an optically bistable system**

The curve illustrated in Fig. 1.1 is an example of hysteresis behavior; that is, the present output of the system depends not only on the present input, but also the history of inputs to the system. Hysteresis behavior is an important and desired characteristic of switching devices because it adds to system stability. Without hysteresis, small fluctuations in the input power could lead to significant, unstable and unwanted fluctuations in the output power. Designing a system such as a switch with hysteresis behavior helps the system stay at a desired output, increasing the stability of the two stable outputs.

# 2. THEORY

The quantum confined stark effect (QCSE) is an electroabsorption effect that occurs in multiple quantum well (MQW) structures when applying an external electric field in the direction of electron confinement; i.e. perpendicular to the multiple layers. QCSE can be exploited to selectively control the absorption of a MQW device, allowing it to be used as an electroabsorption modulator with favorable characteristics such as high speed, high extinction ratio, and low drive voltages [4]. In this chapter I will build a background on quantum wells and MQW structures, as well as discuss how these structures can be manipulated to take advantage of QCSE.

## 2.1 Quantum Wells and MQW Structures

In the context of photonic devices, quantum wells can be constructed by creating special heterostructures, effectively sandwiching a semiconductor material (such as GaAs) between two layers of a different semiconductor material with a wider bandgap (such as AlGaAs; ideally the band gap difference should be large enough such that electron tunneling between layers is limited). Quantum wells are established in a particular kind of heterostructure, in which the center layer is known as the "well" and the outer layers can be referred to as the "barrier" layers; the center layer is referred to as a "well" since electrons will occupy much lower energy states than in the barrier layers, producing a one-dimensional rectangular potential well. A quantum well is a special case of heterostructure in that the well layer must be very thin (comparable to or smaller than the de Broglie wavelength of a thermalized electron) such that the carriers (electrons and holes) are confined in one direction [4]. This heterostructure is called a "quantum well"

since the layer thickness is small enough such that the quantized energy of the electrons within must be satisfied – that is, they may only occupy discrete energy levels to satisfy the standing wave conditions in the well [4; 5].

These discrete energy levels can be calculated by considering a one-dimensional (taken as the z-direction), time-independent form of Schrödinger's equation:

$$\frac{-\hbar^2}{2m}\frac{d^2\varphi_n}{dz^2} + V(z)\varphi_n = E_n\varphi_n \tag{2.1}$$

where m is the electron's effective mass, $\varphi_n$ is the eigenfunction for the nth solution to the equation, and $V(z)$ defines the potential well to which the particle is confined. Assuming an infinite potential well of width $L$ (i.e. $V(z) = 0$ for $0 < z < L$, and $V(z) = \infty$ elsewhere), the solution to equation 2.1 is in the form:

$$E_n = \frac{\hbar^2(n\pi/L)^2}{2m} \tag{2.2}$$

In reality the quantum well will be a three dimensional layer of material that is very thin in one direction (tens of nanometers), but effectively infinitely large in the other directions. Carriers in a quantum well are not confined in three directions, but are free to move in the plane of the quantum well layer itself. As a result the electrons and holes are not confined to discrete energy states, but rather small subbands around the energies calculated by equation 2.2 [5].

Several different methods exist for fabricating these quantum wells in semiconductor devices; perhaps the most common of which is molecular beam epitaxy (MBE) [6]. MBE is a technique which utilizes a very high vacuum environment and ovens from which beams of the desired materials (Al, Ga, and As in the case of AlGaAs/GaAs heterostructures) emerge and are incident upon a heated substrate. Opening and closing shutters to each individual oven is used to control

which material is deposited on the substrate, and the temperature of each oven can be changed to control the amount of each material [5]. Through this method it is possible to create alternating layers of different crystal structures (such as AlGaAs/GaAs/AlGaAs), resulting in what are known as (under the correct conditions) multiple quantum well (MQW) structures [4].

MQW structures are repeated quantum well heterostructures fabricated such that there is no significant electron wavefunction penetration from one quantum well to the adjacent quantum wells [6]. MQW structures can be fabricated to have anywhere from just a few layers to hundreds of layers. The bandgap difference between well and barrier layers, as well as the distance between adjacent quantum wells must be large enough such that adjacent wavefunctions do not disturb one another; otherwise the MQW device will behave as a "superlattice structure", and the discrete MQW absorption subbands will devolve into superlattice minibands [4]. A schematic of a GaAs/AlGaAs MQW structure is included in Figure 2.1.

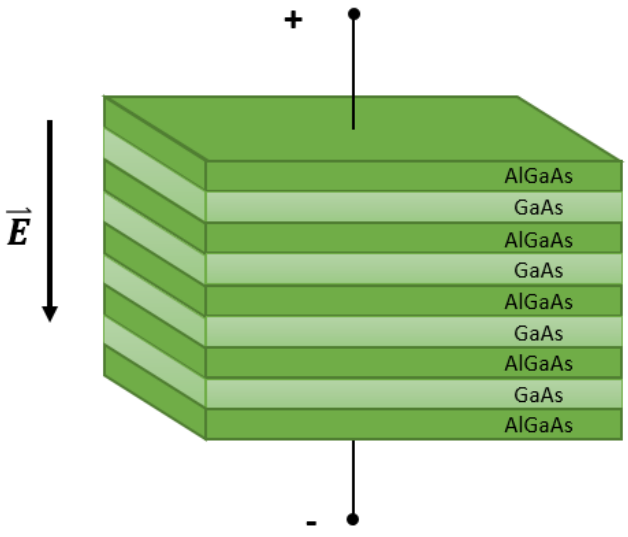


**Figure 2.1: Schematic of a MQW structure with electric field applied perpendicular to the layers, in the direction of confinement.**

## 2.2 The Quantum Confined Stark Effect

When an electric field is applied parallel to the surface normal of the layers (i.e. in the direction of carrier confinement) in a MQW device as in Fig. 2.1, there is a resulting shift in the peak of the structure's optical absorption spectrum, as well as a decrease in the overall absorption; this is what is referred to as QCSE. Applying an electric field effectively shifts the electron states to lower energies while also shifting the hole states to higher energies, thereby reducing the overall energy difference between the conduction band and valence band. This results in a smaller bandgap, as illustrated in the energy-band diagrams in Fig. 2.2.

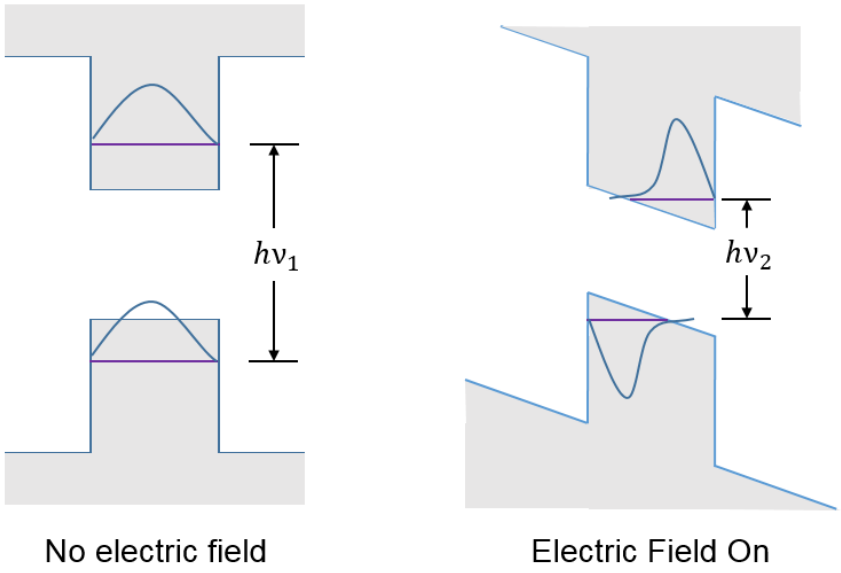


**Figure 2.2: Energy band diagram showing the effect of an applied electric field on the quantum well. Notice that the bandgap energy to decrease ($h\nu_1 < h\nu_2$), and the wavefunctions to shift to opposite sides of the well [4].**

This decrease in bandgap energy correlates to a peak in the absorption spectrum shifting to a longer wavelength. The decrease in energy difference is proportional to the strength of the electric field applied – that is, a stronger electric field will result in a smaller interband energy

difference. In Fig. 2.2 it can also be seen that the wavefunctions for electron and holes shift in opposite directions from the centers of the well. Since the strength of optical absorption is proportional to the overlap integral of conduction and valence envelope wavefunctions, this will result in an overall decrease in total optical absorption [5]. These effects can be seen in D. A. B. Miller's work, Figure 1 [7].

### 2.3 The Self-Electro-Optic Effect Device and Symmetric SEED

A device in which a reverse-biased MQW structure was used to create optical bistability was created and demonstrated by David Miller et. al., which was called the self-electro-optic effect device (SEED) [8]. This device utilizes a reverse-biased p-i-n structure with a MQW structure in the intrinsic region, connected in series with only a resistor. A diagram of the SEED circuit is included below in Fig. 2.3.

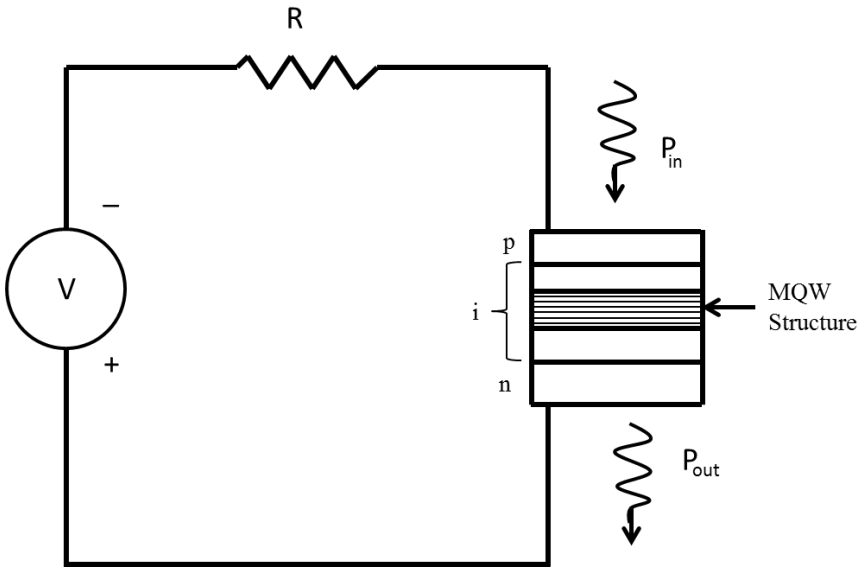


**Figure 2.3: Diagram of the SEED, a device first proposed to produce optical bistability.**

Light is injected into the MQW device, resulting in a photocurrent. By controlling the power of the light, $P_{in}$ , the voltage dropped across the p-i-n structure is effectively controlled. When the optical power into the device is sufficiently low enough, most of the voltage drop occurs across the p-i-n structure. Increasing the optical power proportionally increases the photocurrent produced by the device, in turn increasing the voltage drop across the resistor and decreasing the voltage dropped across the MQW structure. As discussed previously, a change in voltage across a MQW structure leads to a shift in the absorption bands, and thus a change in the overall absorption. When sufficiently modulated light was injected to the device, the result was a bistable optical output leaving the device; this device essentially worked as an optical switch. However, this was only the first device of its kind, and significant changes and improvements were eventually demonstrated.

Several years after the demonstration of the first SEED, Anthony L. Lentine et. al. demonstrated a slightly more complex device with some more favorable performance characteristics: the symmetric self-electro-optic effect device (S-SEED) [7]. This device consisted of two identical reverse-biased, series-connected p-i-n structures with MQW intrinsic regions; a diagram is included below in Fig. 2.4.

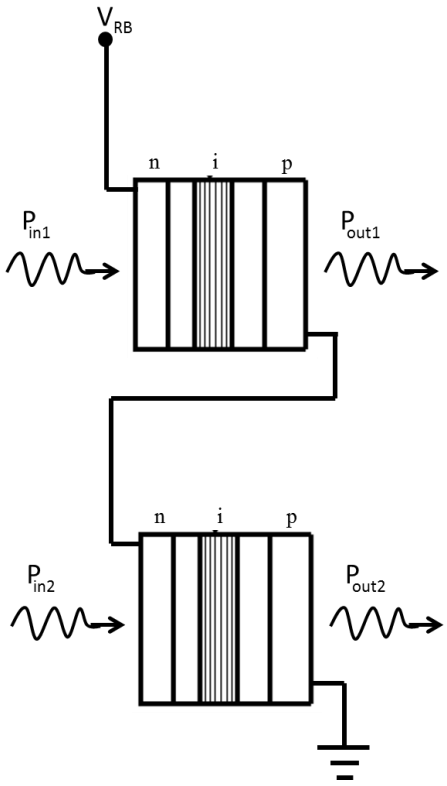


**Figure 2.4: Schematic of the S-SEED.**

The group found that by changing the optical powers $P_{in1}$ and $P_{in2}$ relative to one another, the voltage across each device would switch between two stable states: when the power $P_{in1}$ was greater than the power $P_{in2}$, almost all of the voltage was dropped across the lower p-i-n structure in Fig. 2.4. Conversely, when $P_{in1}$ was lower than $P_{in2}$, the voltage was dropped almost entirely over the upper p-i-n structure. Once again, QCSE leads to a shift in the absorption bands of the MQW structures in the intrinsic region, and consequently a change in the transmission of each device. The result was a device in which controlling the level of light into only one of the devices leads to a change in the light out of both devices, one with an inverted light output respect to the input light, and the other with a non-inverted response.

In order to understand the limitations of an S-SEED device, consider that switching speed is dictated by the time it takes to charge the capacitance of the p-i-n structures [7]. When the current is considered in between the two nodes, Kirchoff's current law shows that,

$$P_{in1}S(V) - P_{in2}S(V_{RB} - V) + C_{diode1}\frac{dV}{dt} - C_{diode2}\frac{d(V_0 - V)}{dt} = 0 \quad (2.2)$$

where $C_{diode}$ is the capacitance of one of the p-i-n structures, $P_{in1}$ and $P_{in2}$ represent the optical power coupled into the top and the bottom diode in Fig. 2.5 respectively, $S(V)$ is the responsivity of the top diode at voltage $V$ across the diode, and $S(V_{RB} - V)$ is the responsivity of the other diode. Assuming the responsivities are constant (realistically they won't be, since QCSE dictates that the absorption will change as a function of the voltage across the MQW structure; but this assumption is made to make calculations simpler) and assuming the diode capacitances are equal, solving for the switching time gives

$$\Delta t = \frac{C_{total}V_{RB}}{S(P_{in2} - P_{in1})} \quad (2.3)$$

where $\Delta t$ is the switching time, and $C_{total}$ is the total capacitance of the coupled device. It is important to note that the switching time is proportional to the total device capacitance, and inversely proportional to the amount of optical power into the device. In order to achieve switching speeds in the GHz range, minimizing diode capacitance while optimizing the amount of power coupled into the system is of prime importance.

This S-SEED served as the inspiration for the symmetric SOA device used in this project. The basis of operation is identical, as discussed in Section 2.4.

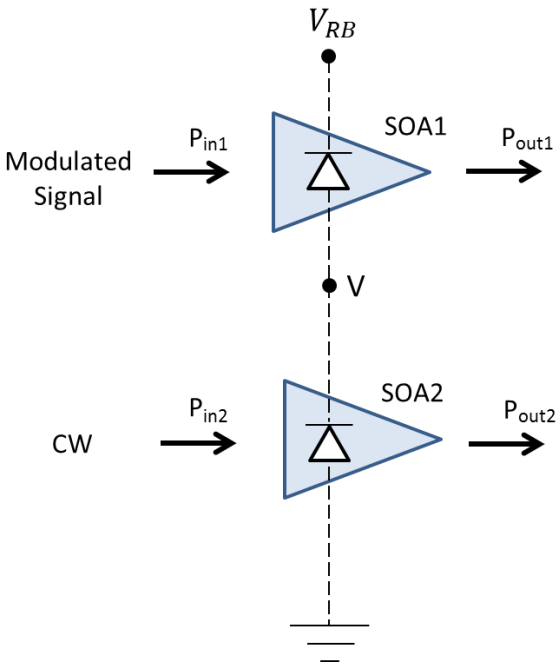


**Figure 2.5: Schematic of the Symmetric SOA Device**

## 2.4 Symmetric SOA Device Operation: Exploiting QCSE to Achieve Optical Switching

In this thesis project, a device containing two series connected SOA MQW structures are placed in reverse bias, and an optical signal is inserted into each waveguide – one input is an optical signal from a constant wave (CW) laser, while the other is a sinusoidally modulated optical signal. A diagram illustrating this is included in Fig. 2.6; the similarities to the S-SEED discussed above are immediately apparent. In this case SOAs serve as reverse-biased p-i-n structures with MQW intrinsic regions.

In order to fully understand the principle of electrical bistability upon which the switch operates, we can consider the load lines for the SOAs. The load line for a reversed bias SOA is essentially equivalent to that of a reverse-biased diode. A diagram of the load lines in the system is included in Fig. 2.7 below. The single solid line represents the load line for SOA2, while the

three dashed load lines represent the cases for which the power into SOA1 is less than the power into SOA2, the power into SOA1 is equal to the power into SOA2, and the power into SOA1 is greater than the power into SOA2 (a higher input power will generate a proportionally greater photocurrent, so the highest load line represents the highest input power). The stable points of system operation occur where the lines intersect, and are represented by circles in Fig. 2.7 (a), and in Fig. 2.7 (b). The squares in both cases represent unstable points of operation.

Assume a varying optical signal is entering SOA1–that is, a sinusoidal optical signal whose amplitude varies above and below the level of power into SOA2. Also assume a CW laser is incident upon the input SOA2. Consider the case when P1 is less than P2; starting with the lowest load line in Fig. 2.7 (a), it can be seen that when the power into SOA1 is lower than the power into SOA2, the system operates at the leftmost intersection point. At this point the voltage V across SOA2 is nearly zero, which in turn means the power across SOA1 $(V_{RB} - V)$ is nearly $V_{RB}$. When P1 increases so that it is equal to P2, operation of the system is then represented by the leftmost intersection of the solid load line and dashed load line 2. It can be seen that at this point, the voltage V across SOA2 is still nearly zero, but is increasing, while the voltage across SOA1 is still nearly $V_{RB}$, but decreasing. Finally, when the power into SOA1 has increased to the point that it is greater than the power into SOA2, the system's operation is represented by the rightmost intersection point in Fig. 2.7 (a). At this point, the voltage has switched to the other stable state; the voltage V across SOA2 is now essentially equal to $V_{RB}$, while the voltage across SOA1 is nearly zero.

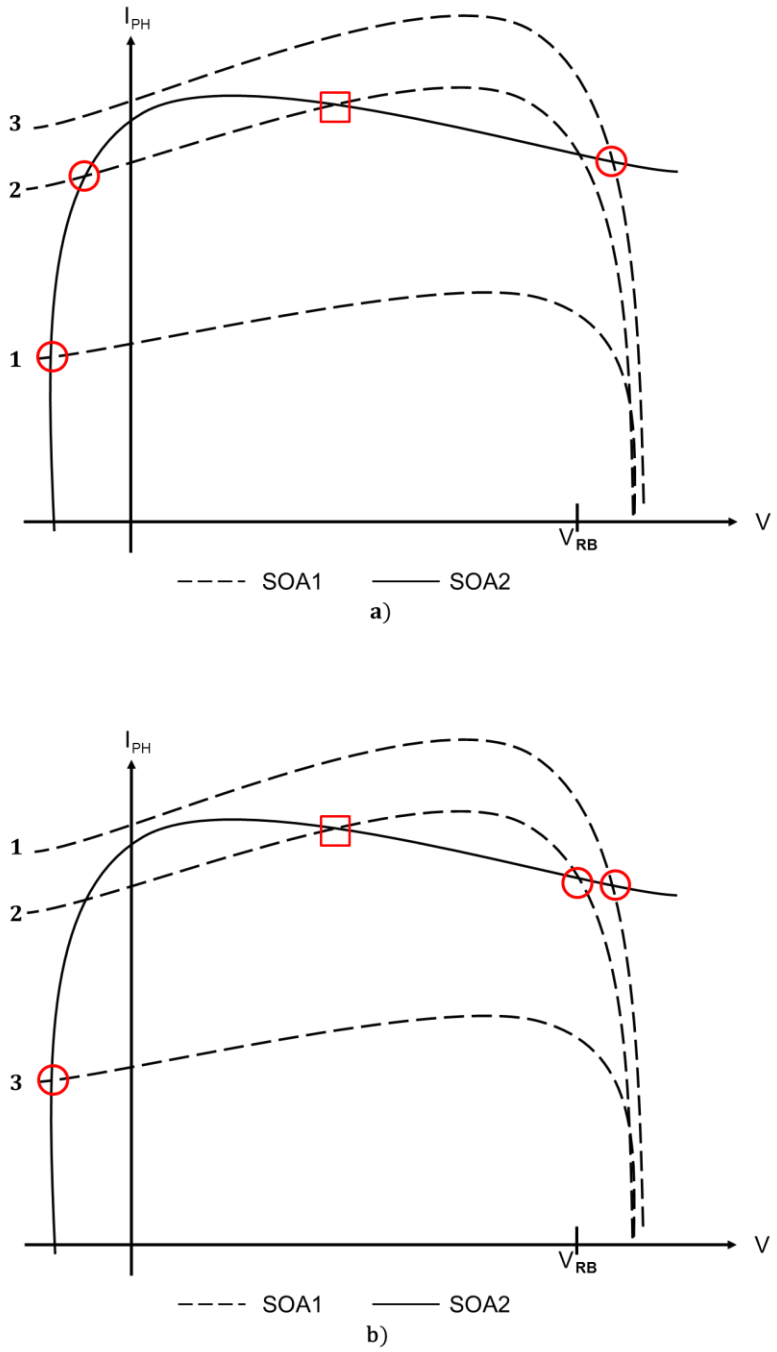


**Figure 2.6: Load lines demonstrating the electrical bistability of the symmetrically coupled SOA device a) when the power into SOA1 is increasing, and b) when the power into SOA1 is decreasing**

Now consider the optical power into SOA1 is decreasing from the upper state, as in Fig. 2.7 (b). When P1 decreases such that it is once again equal to P2, the system operates at the

intersection on the right for the solid line and dashed line 2. In this case the voltage V across SOA2 is still nearly $V_{RB}$, while the voltage across SOA1 is still nearly zero. This shows the electrical bistability of the system. Even though P1 is once again equal to P2, as it was with the intersection of the solid line and dashed load line 2 in Fig. 2.7 (a), the voltage state is different. When the power further decreases to a point where P1 is less than P2 again, the state of system operation switches back to its initial stable state, where the voltage V across SOA2 is nearly zero and the voltage across SOA1 is once again nearly $V_{RB}$.

To summarize, as the power into SOA1 fluctuates above and below the power into SOA2, the system switches between two stable states of operation due to electrical bistability. In one of these states nearly the entire voltage drop of $V_{RB}$ is across SOA2, while in the other case nearly the entire voltage drop is across SOA1. This electrical bistability, coupled with a shift in the SOAs' absorption bands, and consequently a change in the effective transmission of each SOA due to QCSE, also leads to an optically bistable system.

## 2.5 Motivation for Thesis

This configuration of symmetrically coupled, reverse biased SOAs was first demonstrated by M. Gehl, P. Costanzo-Caso, S. Granieri, and A. Siahmakoun, as an analog to the S-SEED and was referred to as S-SOAD [1]. The device was demonstrated to exhibit simultaneous electrical and optical bistable outputs, with both inverted and non-inverted hysteresis behavior with respect to the modulated optical signal. Experiments were demonstrated up to switching speeds in the megahertz range, but were unable to achieve higher rates. It was concluded that the system was limited by external parasitic capacitance and inductance in the interconnection of the SOAs,

since the device was constructed using commercially available parts. An equivalent circuit model, however, suggested that if the capacitance could be reduced to tens of femtofarads the device could exceed 10GHz in switching speeds.

For this thesis, a coupled SOA device was specially made and integrated onto a small platform in order to minimize the parasitic capacitance in hopes of increasing the impedance-limited switching speed.

# 3. DEVICE STRUCTURE AND PREPARATION

This chapter will give an overview of the integrated coupled SOA device and the preparation necessary for the device to operate. Section 3.1 will introduce the device structure, Section 3.2 will outline the device preparation procedures, and Section 3.3 will present the fiber alignment and electrical probing system set-up.

## 3.1 Device Structure

Since the SOA had to be specially designed to achieve high switching speeds, an integrated device had to be fabricated in order to meet these requirements. Three samples of this device were ultimately fabricated at Tampere University of Technology in Tampere, Finland. These integrated, coupled SOA devices were specifically designed to minimize capacitance in order to maximize the rate at which the voltage could switch between the two stable states. As a result, the device had to be very small, and all interconnecting electrical connections had to be kept to a minimum. A picture of one of the physical devices taken under microscope is included in Fig. 3.1, showing the scale of the device – the chips are separated by 882.29 ± 5.32μm. An annotated diagram of the device is included in Fig. 3.2.

The SOAs are made of InP, and are mounted on separate, electrically isolated, gold plated, vertically offset stages. The p-i-n structures are both mounted with the p contact up, and the n-contact mounted to the stage. Gold wire bonds connect the stage upon which the upper SOA (referred to as SOA2) to the top of the lower SOA (referred to as SOA1), effectively creating an electrical connection between the n-contact of SOA2 and the p-contact of SOA1. The waveguides are angled 7° from normal incidence with the edge of each chip, in order to prevent reflection of light back into the SOA waveguide.

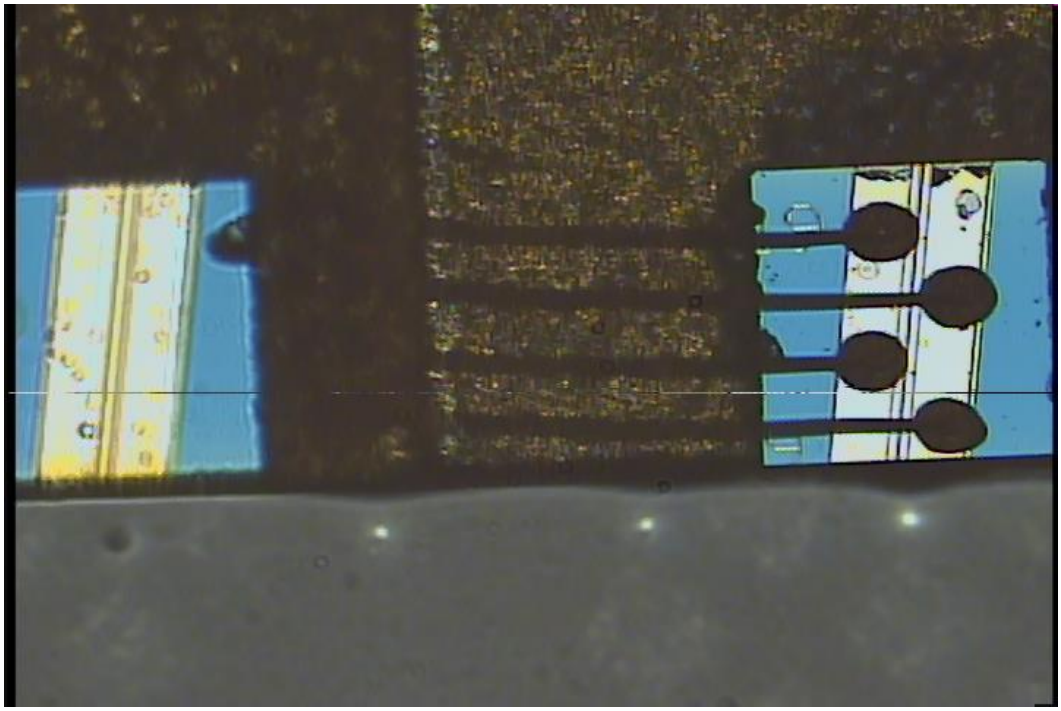

**Figure 3.1: Microscope image of the coupled SOA device**

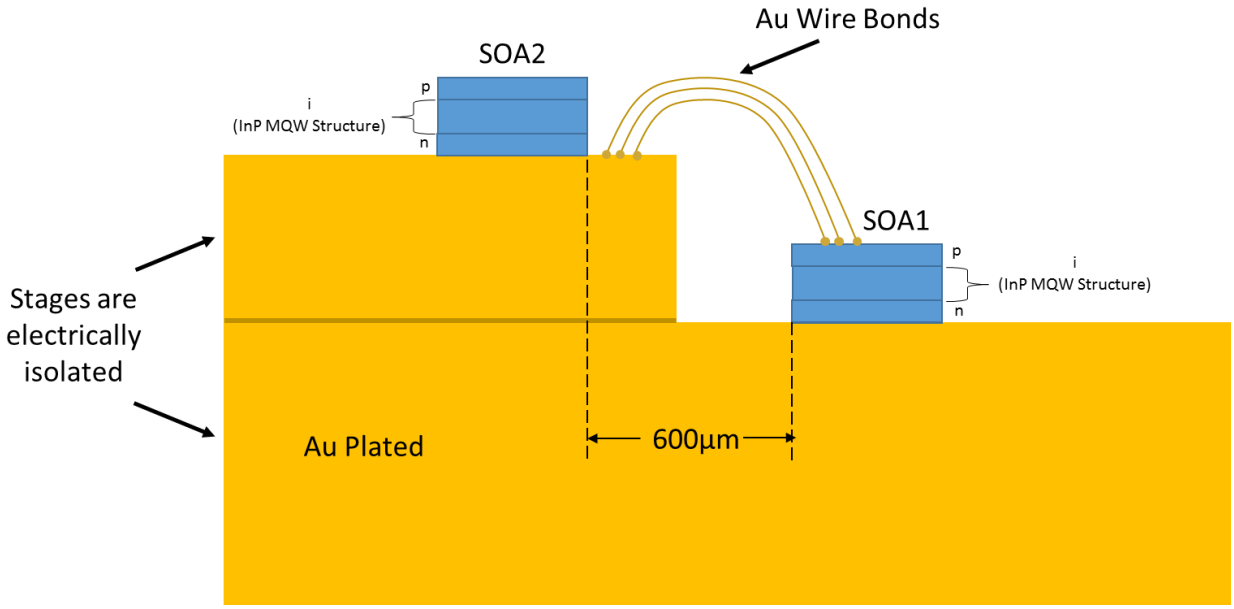


**Figure 3.2: Annotated side-view diagram of coupled SOA device**

A diagram of the SOA waveguide structure is included in Fig. 3.3. The waveguide is fabricated with four 6 nm AlGaInAs quantum well layers, spaced by barrier layers of of AlGaInAs. The ratio of Al:Ga:In:As is different for the quantum wells and the barrier layers such that the band gap of the quantum well material is lower than the band gap of the barrier layer. Total waveguide thickness is 200 nm, and its total width is 2 μm. The waveguide cladding is fabricated from InP. More specific information about material composition and dimensions were not made available from the supplier.

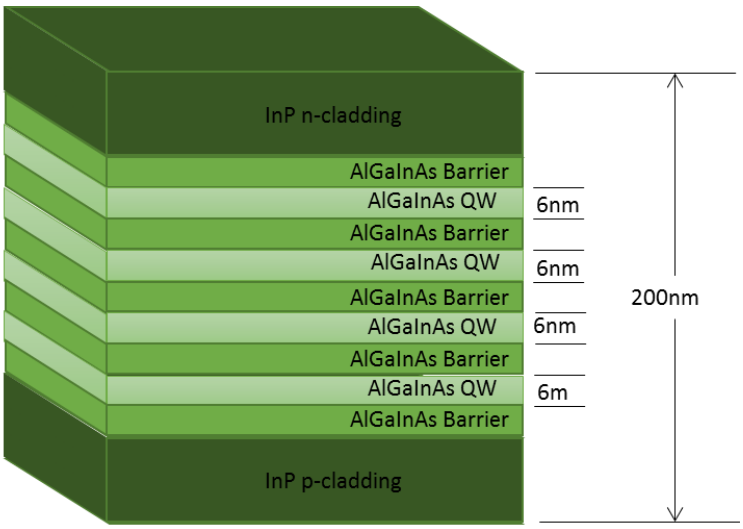


**Figure 3.3: Diagram showing the structure of the waveguide and MQW in the SOA**

Looking at Fig. 3.2, it can be seen that initially there is no way to safely connect an electric probe to SOA2 in order to bias the devices. Placing a manipulator probe directly onto the top of the SOA is very risky – if the device were to be scratched by the probe, it is possible that this would cause substantial loss in the waveguide, leading to significantly less absorption and potentially ruining the device. Additionally, the device must be mounted to a heat sink in order

to help prevent failure due to overheating. These device preparation steps are outlined in the following section.

### 3.2 Device Preparation: Heat Sink and Wire Bonding

To prevent overheating, the coupled SOA device was mounted to a heat sink using a two-part epoxy. The process was very simple, and consisted of mixing the epoxy, applying the epoxy to the heat sink, then using tweezers to seat the device on the heat sink. Extra care had to be taken to apply the epoxy evenly and to place the device so that it was sufficiently level when the epoxy dried. The mounted device was then left overnight to dry. A picture of the result is included below in Fig. 3.4.

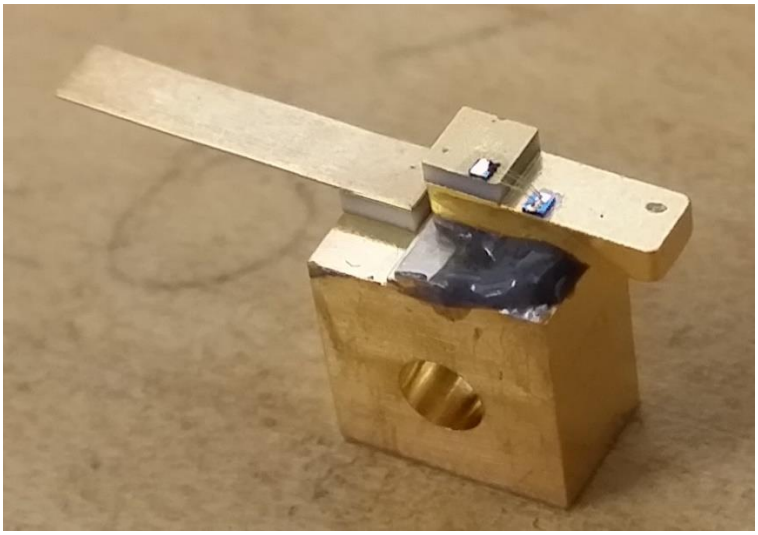

**Figure 3.4: Picture of coupled SOA device successfully mounted to heat sink**

In Fig. 3.4, an electrically isolated cantilever attached to the heat sink can be seen on the left side. Gold wire bonds would later be used to connect this cantilever to the p-contact of SOA2. The result is an electrically isolated surface which can be contacted with a voltage probe on a manipulator to supply voltage to the top of SOA2 without the risk of scratching the SOA. In order to place the gold wire bonds from the SOA to the cantilever, the device was processed using a K&S wire bonder, pictured in Fig. 3.5. The device was placed in a clamp under the wire bonder, on a heated stage. This is pictured in Fig. 3.6.

**Figure 3.5: Picture of K&S manual wire bonder used in wire bonding coupled SOA device to heat sink contact**

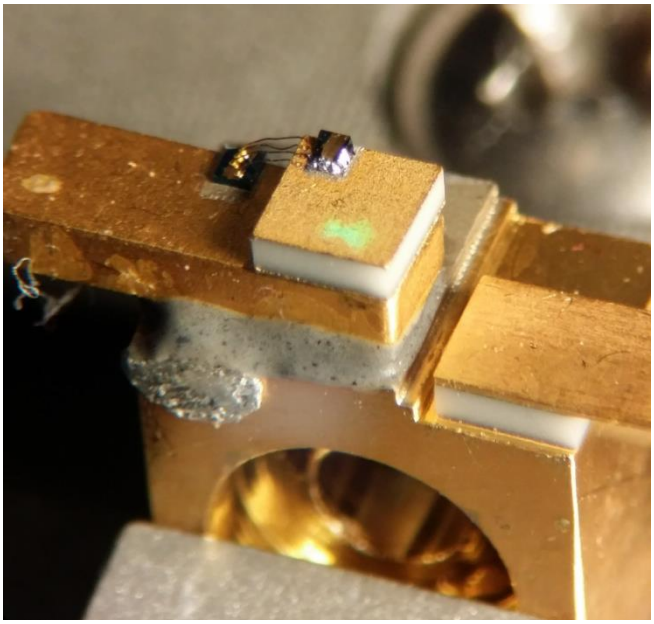

**Figure 3.6: Microscope picture of the coupled SOA device being held under the wire bonder with the clamp**

The particular method of wire bonding used in this case is called ball bonding [9]. In this ball-bonding procedure, a pair of tweezers is used to guide a 25μm gold wire through a small hole in what is called the capillary. Once the wire is successfully fed through the capillary, using what is called the electronic flame-off (EFO) wand, the tip of the gold wire is melted, forming a ball on the end of the wire – this is illustrated in Fig. 3.7 (a). After the ball is formed, the wire retracts so that the top of the ball is in contact with the tip of the capillary. The wire bonder then lowers the capillary until the gold ball makes contact with the desired surface – in this case, the p-contact of SOA2. After a combination of heat from the heated stage holding the device and ultrasonic energy provided by the wire bonder, a ball bond is formed on the SOA. This stage of the process is illustrated in Fig. 3.7 (b). The capillary is then raised and the clamped device is moved so that the capillary is now directly over the desired surface for the second bond to the

cantilever. As the capillary is moved away from the first bond site, the gold wire is allowed to feed through the capillary, forming a loop of gold wire. Once the capillary has been correctly positioned above the second bond location the wire bonder once again lowers the capillary until the gold wire is in contact with the surface. Once again, a combination of heat and ultrasonic energy cause the gold wire to bond to the surface. The capillary then rises from the bond site, but this time a wire clamp prevents more gold wire from passing through the capillary. As a result, the excess wire tears from the second bond site, leaving a loop of gold wire between the two desired surfaces, which in this case is the top of SOA2 and the cantilever of the heat sink. This step is illustrated in Fig. 3.7 (c). This process is then repeated several times for redundancy, to reduce the chance of broken wires or poor contact preventing device operation.

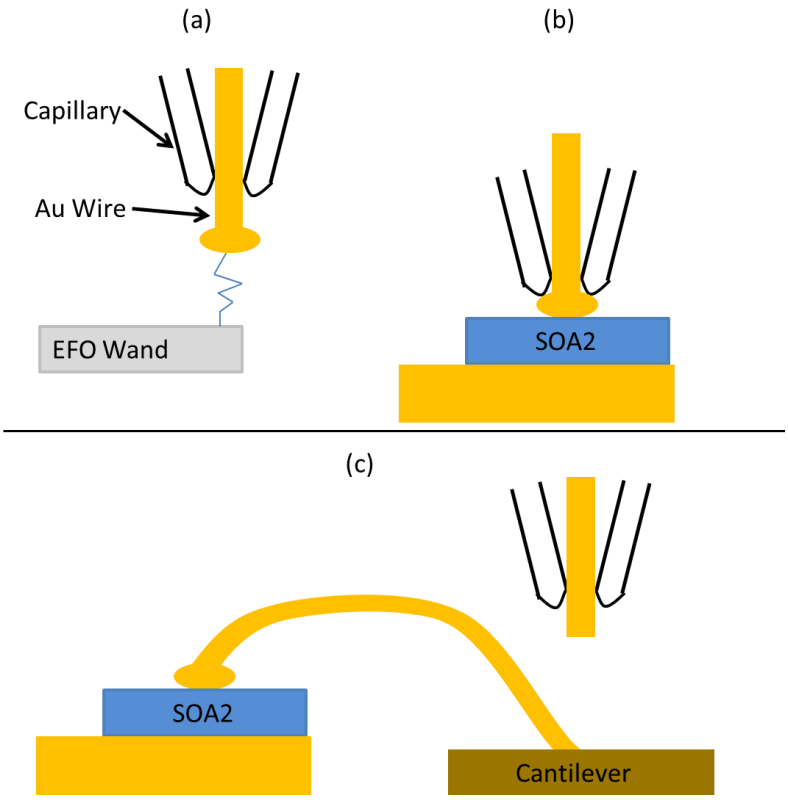


**Figure 3.7: Illustration of ball bonding process**

Even though the bonds between the SOA and the cantilever were successful, the wires were not straight, as seen later in Fig. 3.14. The bonding sites are separated by a significant vertical distance, making it difficult to connect the wire from SOA2 to the cantilever without touching the gold plated stage.

### 3.3 Impedance Measurements

As discussed in Section 2.3, the maximum switching speed of a symmetrically coupled MQW device structure is dictated by the time it takes the diodes can charge and discharge. This switching time is directly proportional to the diode capacitance, as indicated in equation 2.3. To calculate the impedance limited switching capabilities of this SOA, it was necessary to measure the capacitance of p-i-n structures. Impedance measurements were conducted using a Gamry Reference 600 potentiostat/galvanostat/ZRA with Gamry EChem Analyst software. Electrical leads from the Gamry device were connected to electrical probes, and measurements were made over SOA1.

In order to analyze the measurements, an equivalent circuit model had to be built and data fit to this model in the Gamry EChem Analyst software. The equivalent circuit model in Fig. 3.8 was used for fitting the data taken from the SOA. This circuit consists of a series resistor and inductor along with parallel resistor and capacitor. This model was adapted from equivalent circuit models that have been used to analyze the frequency response of MQW devices [19, 20].

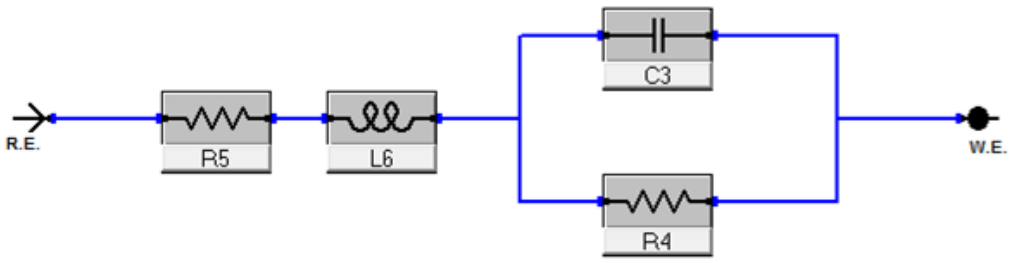


**Figure 3.8: Equivalent circuit model used in measuring diode capacitance**

The data collected in EChem Analyst software complete with fit and measured impedance values are included in Fig. 3.9. The capacitance was measured as 13.10fF, suggesting system is suitable for gigahertz frequency operation [1]. The software listed a goodness of fit of 2.550E-3, indicating a good fit.

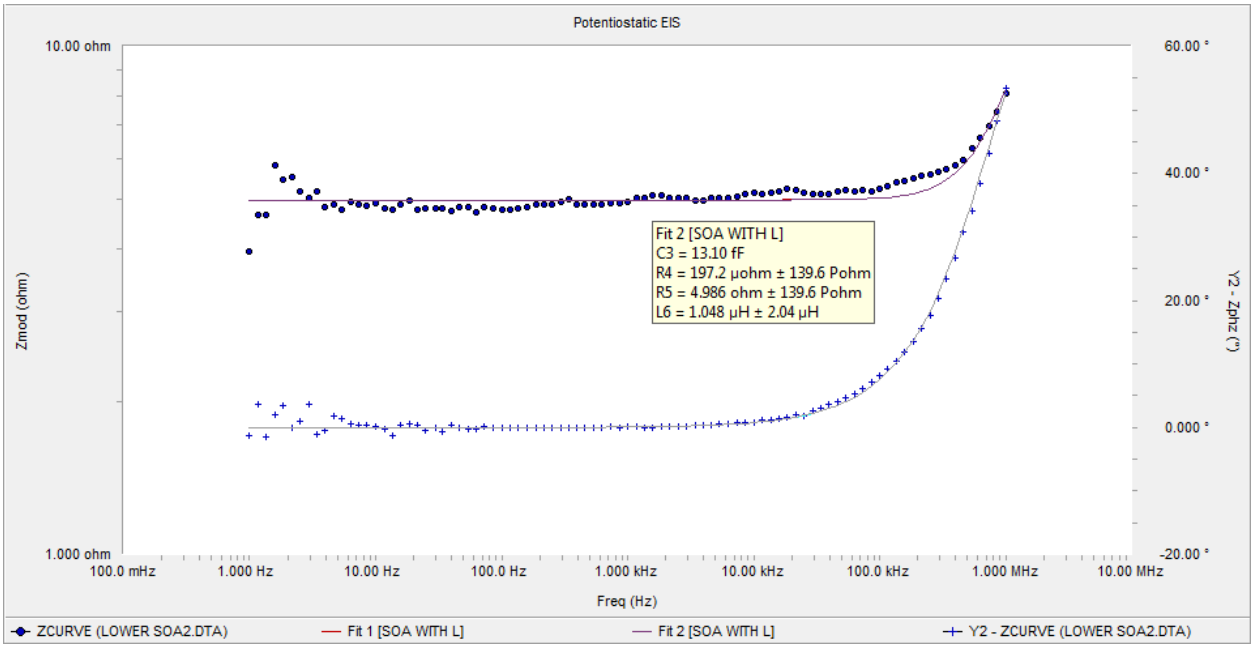


**Figure 3.9: Impedance measurements from Garmy EChem Analyst software**

### 3.4 Optical Fiber Alignment System and Electrical Probing

When preparing the device for experimentation, it was determined that four optical fibers and three electrical probes were necessary to sufficiently observe the switching operation. The four optical fibers are needed to couple light into and out of the two SOAs. Three fibers could be used, since it is only necessary to observe the optical output of one SOA at a time, but it is mandatory that both SOAs have light coupled into them. Three electrical probes were necessary to supply voltage to the device, as well as monitor the voltage, V, across SOA2 (see diagram in Fig. 2.6). A top-down drawing of the required components positioned on the coupled SOA device is included in Fig. 3.10. Standard 9μm core single-mode optical fibers are cleaved and aligned to couple light in this setup.

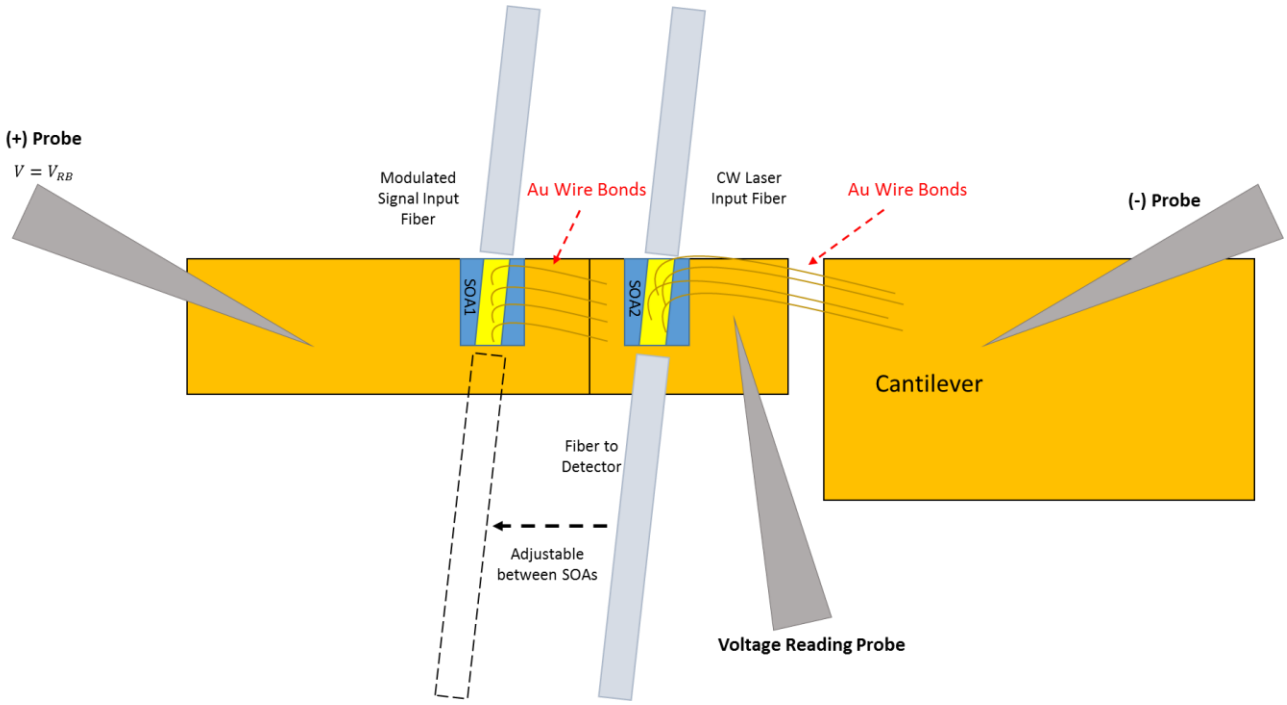


**Figure 3.10: Top-down schematic of all probes and fibers necessary to observe switching operation**

In order to position the fibers to successfully couple light into and out of the SOAs, a special fiber alignment system had to be built. Traditionally optical fiber translation stages offer five degrees of freedom in movement (x, y, z, pitch, and yaw), but at the cost of being very large. The SOAs on this small device are only separated by 882.29 ± 5.32μm, and since three or four fibers are necessary in this system to couple light into and out of each SOA, a traditional fiber alignment translational stage could not be used as they are too large to fit four fibers in such a small space.

The solution to this issue came in the form of Micromanipulator probes. When selecting electrical probes, it was noticed that the probe tip holder was just the right size to also hold the tight buffer jacket of a standard optical fiber. Since two extra Micromanipulator probes were available, these were ultimately used for fiber alignment. The manipulators allowed the fiber to be moved in x, y, and z directions. The angle with the waveguide had to be set by repositioning the manipulator stage manually, but this was determined to be an acceptable tradeoff for the ability to place two fibers so close together. A bare fiber alignment translational stage was still used for aligning the detection fiber.

The final device probing setup included three voltage probes on manipulator bases to supply bias and measure voltage across SOA2, two optical fibers held with Micromanipulator probe holders to couple light into each SOA, a Newport 561-FH fiber translation stage used to move the detection fiber between the two SOAs, and a vertically mounted digital microscope to aid in fiber alignment. An annotated picture of the entire voltage probing and fiber alignment setup is included in Fig. 3.11.

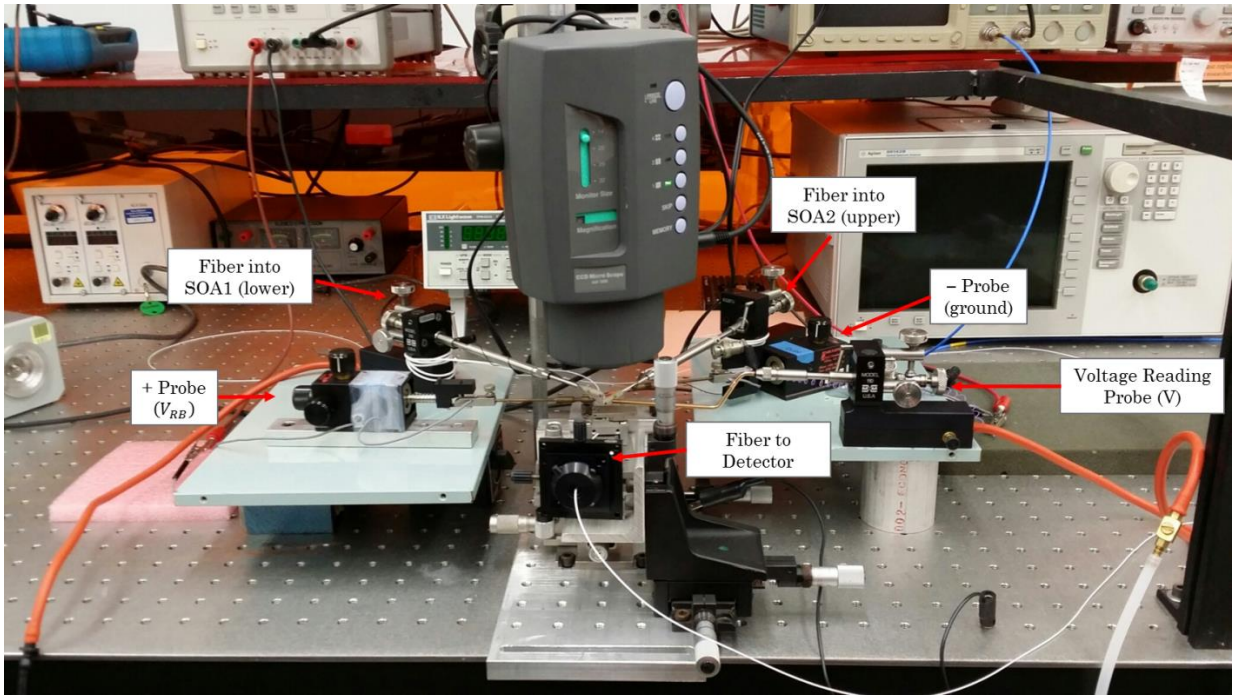


**Figure 3.11: Annotated picture of fiber alignment and voltage probing setup**

The importance of precision in alignment when coupling light between two waveguides has been well documented, even in the early stages of optical waveguide development [10]. Misalignment of waveguides can be classified in three categories: axial displacement, longitudinal separation, or angular misalignment [11]. A diagram illustrating each of these three misalignments are included in Fig. 3.10. Axial displacement occurs when the axes of the optical waveguides are separated by some distance, as in Fig. 3.12 (a). Longitudinal separation refers to the gap between waveguide ends, as illustrated in Fig. 3.12 (b). Angular misalignment is the result of the axes of the two waveguides being separated by some angle as seen in Fig. 3.12 (c).

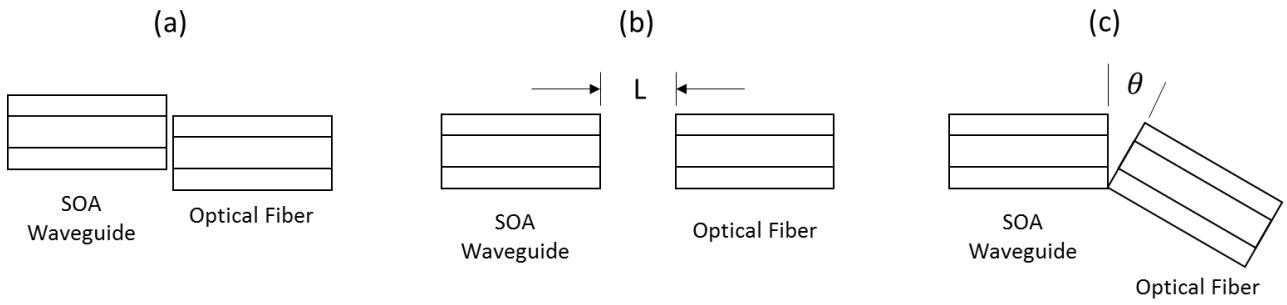


**Figure 3.12: Types of waveguide misalignment**

Of these misalignments, the greatest power loss occurs in the case of axial displacement. Assuming the waveguides have equal numerical apertures, the optical power coupled from one waveguide to the other would be proportional to the common area of the waveguides. In this case, light is being coupled from a cylindrical optical fiber to a rectangular semiconductor waveguide so these assumptions will not provide accurate calculations of loss for the coupled SOA device to the optical fiber. However, the equations will serve as a useful demonstration of how sensitive to misalignment the system will be since the actual system will experience more loss than a fiber-to-fiber coupling system.

In the case of axial misalignment of identical, step-index single mode fibers, the coupling efficiency can be modeled as,

$$\eta = \frac{A_{common}}{\pi a^2} = \frac{2}{\pi}\cos^{-1}\left(\frac{d}{2a}\right) - \frac{d}{\pi a}\left[1 - \left(\frac{d}{2a}\right)^2\right]^{1/2} \tag{3.1}$$

where *a* is the radius of the fiber core, and *d* is the distance of axial separation between the two fibers. Calculations show that even a small displacement will result in significant power loss. For the case of a 9μm diameter core $(a = 4.5\mu m)$ and an axial separation of only 2μm, the coupling efficiency is calculated to be $\eta = 0.719$, corresponding to an insertion loss of -1.43dB.

Thus, even a very small axial misalignment between optical fibers can lead to a substantial decrease in coupling efficiency, and the insertion loss will be even more substantial in the case of coupling light from optical fiber to the rectangular waveguide on the SOA, as explored in Section 3.5.

Angular misalignment, and to a greater extent longitudinal separation, contribute less loss than axial displacement [12]. Rotational stage alignment was not feasible in this setup, since fiber alignment stages with rotation capability are generally very large, so emphasis was put towards minimizing axial and longitudinal displacement between optical fiber and SOA waveguide end. Fiber coupling angle was optimized by manually rotating the micromanipulator base and realigning axial and longitudinal positon.

### 3.5 Coupling Power Loss

In order to get an idea of magnitude of power lost in coupling between the optical fiber and the SOA waveguide, the sources of loss must be considered. Typically the total optical power loss can be calculated in dB as:

$$L(dB) = P_{in} - P_{out} \tag{3.2}$$

$$L(dB) = L_{coupling,in} + L_{coupling,out} + L_{\alpha} \tag{3.3}$$

where $P_{in}$ and $P_{out}$ are the measured optical power entering and leaving the waveguide, $L_{coupling,in}$ and $L_{coupling,out}$ are the coupling losses in dB at the input and output of the waveguide, and $L_{\alpha}$ is the loss in dB due to absorption and scattering in the waveguide. The most significant of these losses is the coupling loss, which can be attributed to two primary causes: the

mode size mismatch between the optical fiber and the waveguide, and Fresnel reflection losses due to difference in index of refraction [13].

To evaluate the power loss caused by mode-size mismatch, it is necessary to calculate the square of the overlap integral of the field profile for the mode leaving the optical fiber, and for the field of the waveguide mode [14]:

$$\eta_{mode\ coupling} = \left( \frac{\iint_{-\infty}^{\infty} |E_{fiber}(x,y,z=0)||E_{waveguide}(x,y,z=0)|\, dx\, dy}{\sqrt{\iint_{-\infty}^{\infty} |E_{fiber}(x,y,z=0)|^2\, dx\, dy \iint_{-\infty}^{\infty} |E_{waveguide(x,y,z=0)}|^2\, dx\, dy}} \right)^2 \tag{3.4}$$

where $E_{fiber}$ is the electric field profile of the mode in the optical fiber, and $E_{waveguide}$ is the field profile of the fundamental mode for the waveguide. The expression above is valid for the region where the coupling between optical fiber and SOA waveguide take place, defined as the position $z = 0$.

The electric field of the fundamental mode propagating in a single mode optical fiber will have a radially symmetric Gaussian profile, and can be modeled as:

$$E_{fiber} = e^{-\frac{(x^2+y^2)}{\omega_0^2}} \tag{3.5}$$

where $\omega_0$ is defined as the beam waist radius, defined in the normalized electric field profile as the distance from the central maximum where the field magnitude has been reduced to $\frac{1}{e}$. In the case of an optical fiber, this value can be related to common characteristic of an optical fiber, the fiber's mode field diameter (MFD). The relation can be defined as follows:

$$MFD = 2\omega_0 \tag{3.6}$$

A plot of the electric field profile for the fundamental Gaussian mode in a single-mode fiber with a 9μm MFD, a typical value for single-mode fiber, is included in 3.13 (a), and a cross section of the field profile depicting the beam waist radius and MFD can be found in Fig. 3.13 (b).

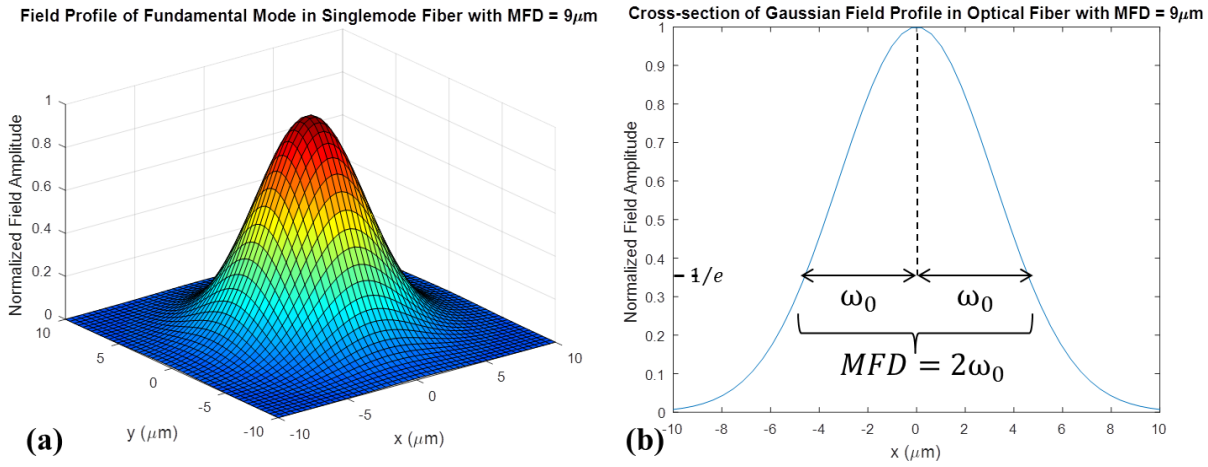


**Figure 3.13: (a) 3D electric field profile of a Gaussian beam in a single-mode fiber. (b) Cross-section of the Gaussian profile illustrating parameters $\omega_0$ and the MFD.**

The field in the SOA waveguide will also take on a Gaussian shape. However since this waveguide is rectangular, not cylindrical and radially symmetric as it was with the optical fiber, the Gaussian function defining the electric field profile will have a different $\frac{1}{e}$ beam waist radius for the x and y directions [14]. The field for the fundamental mode in the rectangular waveguide can be modeled as:

$$E_{waveguide} = e^{-\left(\frac{x^2}{\omega_x^2}+\frac{y^2}{\omega_y^2}\right)} \tag{3.7}$$

For the rectangular SOA waveguide, the values $\omega_x$ and $\omega_y$ will depend on the waveguide materials, dimensions, and structure. Unfortunately specific information about the device structure was not made available by the supplier, so $\omega_x$ will be approximated as half the width of the SOA waveguide and $\omega_y$ as half the height of the waveguide. Figure 3.14 shows plots of the fundamental mode for a rectangular waveguide with these dimensions ($\omega_x = 1\mu m$ and $\omega_y = 0.1\mu m$). In this waveguide the fundamental mode profile is highly asymmetric, unlike in the fiber where the fundamental mode is a radially symmetric Gaussian profile.

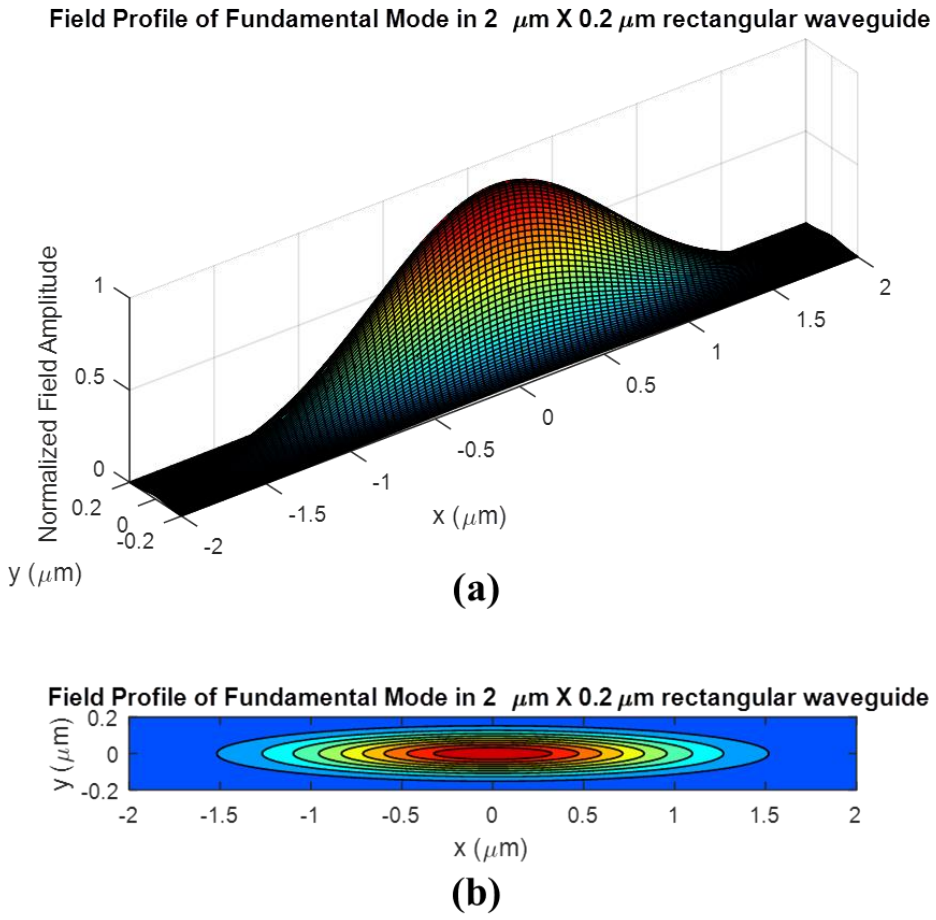


**Figure 3.14: (a) 3D electric field profile of the fundamental mode in the SOA waveguide. (b) Contour plot of electric field profile.**

As expressed in equation 3.4, the power loss in coupling between the two waveguides is defined by the square of the overlap integral between the mode profiles. Figure 3.15 contains mode profile cross-sections for the optical fiber and for both x and y direction in the SOA waveguide. The curves illustrate the discrepancy in the mode size between light in the optical fiber and the SOA.

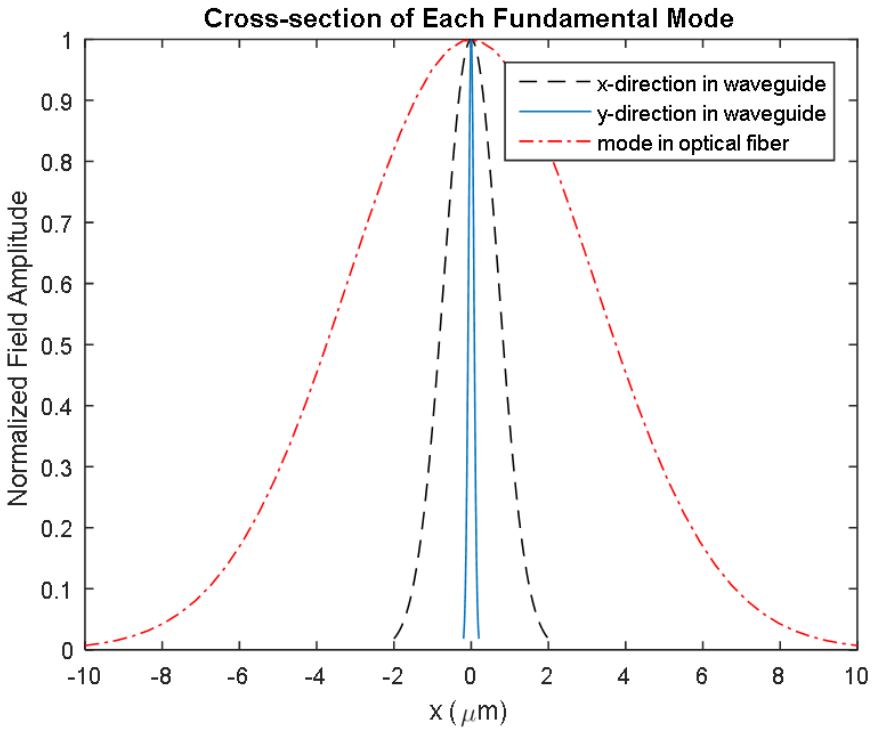


**Figure 3.15: Mode cross sections for both directions in the SOA waveguide and in the optical fiber.**

Evaluating equation 3.4 with the values from equations 3.5 and 3.7, it can be shown that the power coupling efficiency is given by:

$$\eta_{mode\ coupling} = \frac{\frac{4}{\omega_0^2}\left[\frac{1}{\omega_x \omega_y}\right]}{\left[\frac{1}{\omega_0^2}+\frac{1}{\omega_x^2}\right]\left[\frac{1}{\omega_0^2}+\frac{1}{\omega_y^2}\right]} \tag{3.8}$$

Using the physical values for the fiber and for the waveguide as mentioned previously $(\omega_0 = 4.5\mu m, \omega_x = 1\mu m, \omega_y = 0.1\mu m)$, equation 3.8 yields a coupling efficiency of 0.019. Just under two percent of the light leaving the optical fiber is coupled to the SOA. The power loss expressed in dB can be calculated as:

$$L_{mode\ coupling} = -10\log_{10}\left(\eta_{mode\ coupling}\right) \tag{3.9}$$

Equation 3.9 results in a coupling loss of 17.3dB due to mode mismatch.

Accounting for the power loss due to Fresnel reflection is a more straight forward calculation. The reflectance at an interface of two unlike materials is defined as the ratio of optical power reflected to the optical power incident on the interface [15]:

$$R = \frac{P_R}{P_I} \tag{3.10}$$

TM and TE polarized light will experience different reflectance values due to the different boundary conditions at the interface for the two polarizations [15]. The reflectance coefficients depend on the indices of refraction of the material on each side of the interface, as well as the angle of light incidence:

$$R_{TE} = \left|\frac{n_1\cos\theta_i - n_2\sqrt{1-\left(\frac{n_1}{n_2}\sin\theta_i\right)^2}}{n_1\cos\theta_i + n_2\sqrt{1-\left(\frac{n_1}{n_2}\sin\theta_i\right)^2}}\right|^2 \tag{3.11}$$

$$R_{TM} = \left| \frac{n_1 \sqrt{1-\left(\frac{n_1}{n_2}\sin\theta_i\right)^2} - n_2 \cos\theta_i}{n_1 \sqrt{1-\left(\frac{n_1}{n_2}\sin\theta_i\right)^2} + n_2 \cos\theta_i} \right|^2 \quad (3.12)$$

where $n_1$ is the index of refraction for the material from which the light is travelling towards the interface, $n_2$ is the index of refraction for the material into which the light is travelling, and $\theta_i$ is the angle of light incidence, measured from the surface normal to the interface. In the case of unpolarized light, the total reflectance can be calculated by taking the average of equations 3.11 and 3.12:

$$R_{total} = \frac{R_{TM}+R_{TE}}{2} \quad (3.13)$$

Assuming the fiber is not physically touching the SOA, the index of refraction $n_1$ will be that of air, while $n_2$ will be that of the waveguide material, AlGaInAs. The index of refraction of AlGaInAs will depend on the ratio of the elements used in making the material. Since the exact ratio between Al:Ga:In:As is not known for these SOAs, a typical value of 3.4850 will be assumed [16]. Since the optical fiber tip is cleaved at a 90˚ angle, the angle of incidence $\theta_i$ will be the angle formed between the optical fiber and the waveguide surface normal, measured to be $30 \pm 1^{\circ}$. Using these parameters in equations 3.11 - 3.13 yields a total reflectance of $R_{total} = 0.307$. The power loss due to Fresnel reflection at this interface can be calculated as:

$$L_R = -10\log_{10}(1-R) \quad (3.14)$$

For a total reflectance of 0.307, the calculated power lost in dB is 1.59dB at each end of the waveguide.

When the calculated power losses due to reflection and mode mismatch are used in equation 3.3, the result is a total power loss for coupling light into the waveguide of about 18.9dB. Thus,

the coupling of light from a bare, cleaved single-mode fiber into such a small waveguide is a very inefficient process. This great power loss will substantially degrade device switching performance.

### 3.6 Method for Alignment of Optical Fibers for Maximum Power Coupling

In order to assist in alignment of the optical fibers to the SOA waveguides, a vertical microscope was mounted above the setup, and live video was fed to a computer through IC Capture software. This setup allowed the optical fibers to be viewed in real-time while positioning to align with the waveguides. A top-down picture of the aligned optical fibers was taken with the microscope, and is included in Fig. 3.16. Visual alignment of the optical fibers would not prove adequate for obtaining maximum coupling efficiency on its own, however; this would only serve as the first step in system alignment. A quantitative method for improving alignment was necessary to assure optimum power coupling to the SOA waveguide from the optical fiber. This method was realized in the form of measuring spontaneous emission from the SOAs.

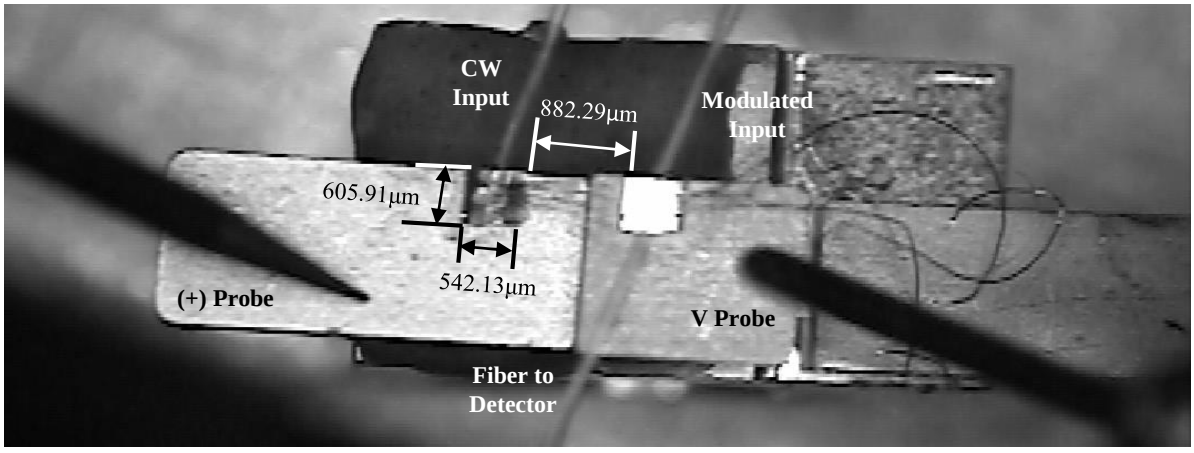


**Figure 3.16: Image of optical fibers aligned with coupled SOA device, all measurements ±5.32μm. Both SOAS measured to same dimensions within uncertainty.**

Similar to semiconductor laser diodes, when a forward current is placed across an SOA, the current causes charge carrier recombination and thus it will emit a measureable spontaneous emission. This spontaneous emission can be used to help align the fibers for maximum power coupling. By measuring the spontaneous emission, and adjusting fiber position until the power coupled out of the waveguide is maximized, the fiber will be aligned for maximum coupling efficiency.

Fig. 3.17 shows a diagram of the electrical probe orientation and setup for the optical fiber alignment procedure. Using an Agilent E3631A DC power supply, the voltage limit is set to 3.000V to prevent damage to the device, and 80mA of forward current is set through the SOAs. Then, one by one, each of the three fibers are plugged into an ILX Lightwave FPM-8210 optical power meter, set to measure power at a wavelength of 1550nm. The fiber position is then fine-tuned by adjusting the fiber manipulators. When the fiber position cannot be adjusted to further increase the optical power measured by the power meter, it has reached the position at which maximum coupling efficiency is achieved. This method proved to work very well for coupling light into and out of the SOA waveguides.

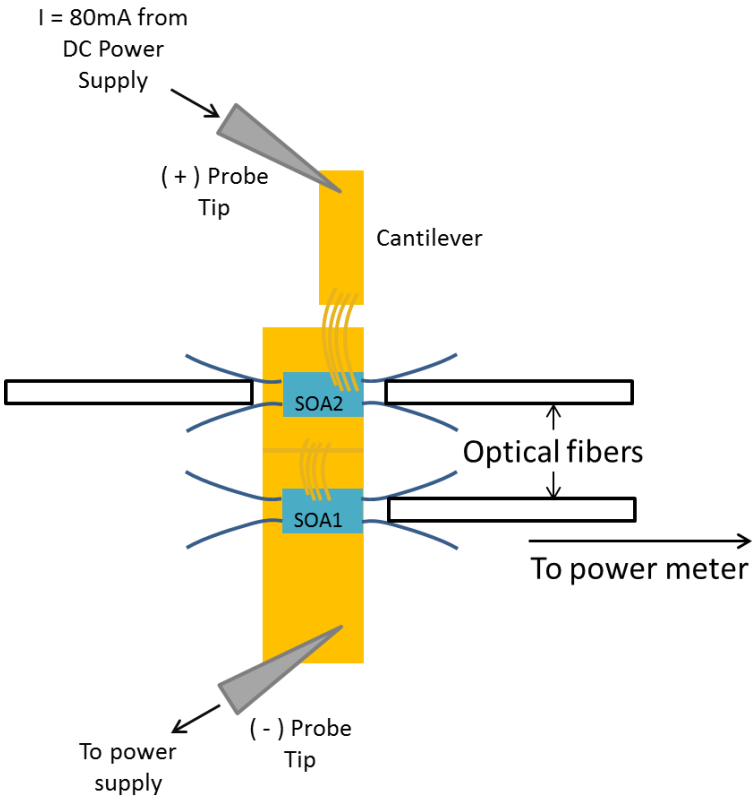


**Figure 3.17: Diagram showing probe orientation and setup of optical fiber alignment method**

# 4. EXPERIMENT SETUP, PROCEDURES, AND RESULTS

This chapter is devoted to outlining the equipment set up, reporting the performance characteristics, and analyzing any experimental results in testing the coupled SOA device. The device was tested in several phases; first, the capacitance of the diode was measured, as reported in Section 3.4. Optical transmission at several wavelengths was then characterized as a function of applied voltage for both of the SOAs to prove QCSE. Bistability and switching behavior is analyzed at low speeds (~1kHz) initially, and finally system performance is analyzed at higher speeds.

## 4.1 Device Impedance Measurements

To evaluate the coupled SOA device's potential for high speed switching, it was necessary to first measure its electrical impedance. The impedance was measured using a Gamry Reference 600 potentiostat with Gamry EChem Analyst software package. In order to accurately measure the device's electrical characteristics, an equivalent circuit model had to be built in the measurement software using resistors, capacitors, and inductors.

Electrical leads were connected to the probes, and Gamry analysis software was used to fit the electrical characteristics data to the equivalent circuit model. The equivalent electrical circuit model, as well as Gamry software measurement outputs, are included Section 3.4. Using this method, it was determined that the diode capacitance is 13.1fF, suggesting that the device is sufficient for impedance-limited switching with speeds in the GHz range [1].

### 4.2 Characterizing Device Transmission: QCSE

Since this system's optical signal is produced by an electro-absorption modulation due to QCSE, it is important that the transmission of SOA2 be characterized at several wavelengths. By determining the wavelength at which the transmission shows the greatest change in response to changing voltage, this procedure will show at what wavelength the system will produce the strongest switching optical signal. This experiment will also serve as a proof of QCSE in these SOAs.

A diagram of the equipment setup for characterizing device transmission is included in Fig. 4.1 below. First, an OptiLab RTL-1550 tunable laser source is plugged into an Amonics AEDFA-C-15B-LCB erbium doped fiber amplifier (EDFA), whose output is sent directly to an Agilent optical spectrum analyzer (OSA). The laser's current setting is set to 300mA, and the tuning bias port is connected to an Agilent E3631A DC power supply so the bias can be adjusted to tune the output wavelength of the laser. Once the tuning wavelength is set, the EDFA's pump laser current is adjusted to reach a desired output level – the pump current was set to 100mA in this case. Table 4.1 includes the tuning bias, laser wavelength, and power out of the EDFA used at each wavelength.

After the initial power out of the EDFA is measured, the optical fibers are aligned with the SOA and the device is connected in reverse-bias. The EDFA output is connected to the launch fiber for the SOA, and the receiving fiber on the other side of the waveguide is connected to the OSA. The reverse bias voltage $V_{RB}$ is adjusted, and the resulting output power is then recorded. This process was repeated for seven different wavelengths; the results are reported in Fig. 4.2, and collected data is included in Appendix A.

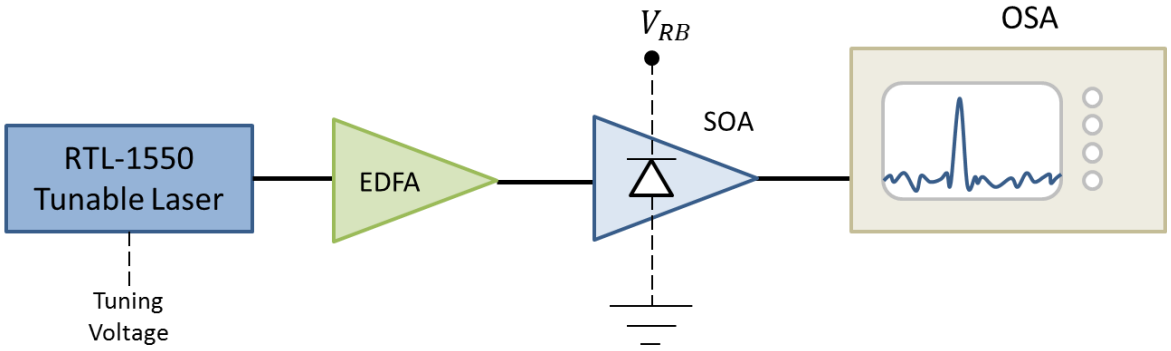


**Figure 4.1: Diagram of equipment setup for characterizing spectral transmission**

| Wavelength (nm) | Tuning Voltage (V) | Power out of EDFA (dBm) |
|---|---|---|
| 1530 | 8.45 ± 0.01 | 7.70 ± 0.01 |
| 1535 | 9.35 ± 0.01 | 8.11 ± 0.01 |
| 1540 | 10.09 ± 0.01 | 6.33 ± 0.01 |
| 1545 | 10.73 ± 0.01 | 7.26 ± 0.01 |
| 1550 | 0.95 ± 0.01 | 7.94 ± 0.01 |
| 1555 | 2.23 ± 0.01 | 8.10 ± 0.02 |
| 1560 | 3.34 ± 0.01 | 6.10 ± 0.01 |

**Table 4.1: Input optical power at each wavelength for testing SOA transmission**

The transmission of the SOA is calculated as the difference between the output power and the input power, defined as:

$$T(dB) = P_{out}(dB) - P_{in}(dB) \tag{4.1}$$

This transmission depends on many factors, such as optical fiber alignment and reflection losses as discussed in Section 3.4, as well as the absorption of the waveguide. However, the only

one of these parameters that will show significant change with applied voltage or input wavelength is the absorption due to QCSE. So the transmission changes in Fig. 4.2 are primarily due to changes in absorption.

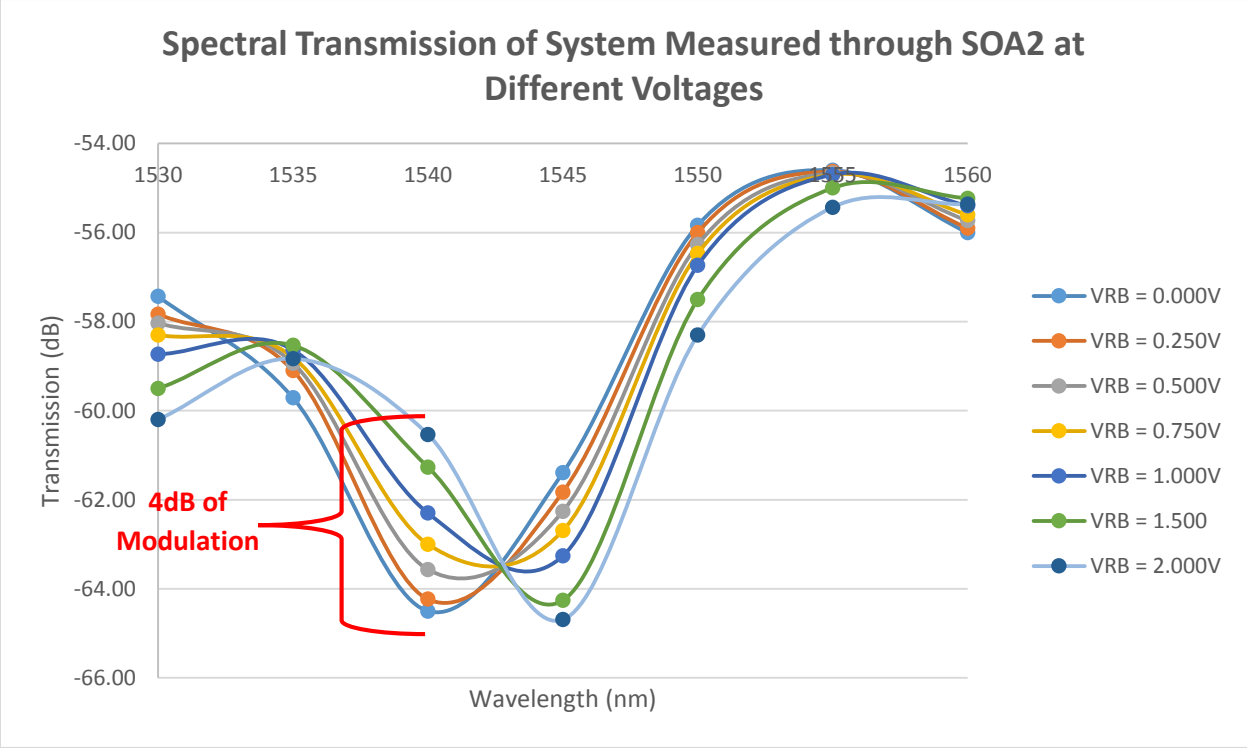


**Figure 4.2: Spectral T(V) measurements for SOA2**

The results shown in Fig. 4.2 match the behavior that is expected with QCSE; as an increasingly higher reverse bias is placed across the MQW structure, a shift of the absorption peaks (the lowest point or valley in the transmission spectrum) occurs, moving in the direction of

longer wavelengths. In this case, the absorption peak shifts from about 1540 nm when the applied voltage $V_{RB} = 0.000V$, to about 1545nm when $V_{RB} = 2.000V$.

The difference in transmission at each point can also be used to tell at which wavelength the RTL-1550 tunable CW laser should operate in order to achieve optimum modulation in the output optical signal out of SOA2. For a reverse bias voltage of 2.000V, tuning the RTL-1550 laser to a wavelength of $\lambda = 1540\ nm$ will result in about 4 dB of optical modulation.

### 4.3 Analyzing Bistability at Low Speeds

Before trying to get the system to switch at high speeds, electrical and optical bistability were observed at lower switching rates in order to get a better understanding of how the device operates. Once switching operation was established at lower speeds, system parameters such as optical power and fiber alignment could be fine-tuned to further increase switching speeds. A schematic of the experimental setup for bistable operation at 1kHz is included in Fig. 4.3.

After optical fibers are aligned by the spontaneous emission measurement method outlined in Section 3.4, a reverse bias voltage, $V_{RB}$, of 2.000V is placed across the coupled SOA device. In this configuration, the modulated optical signal is sent into SOA1. A Fujitsu FLD5F10NP laser diode is connected to the Amonics EDFA, and the output is passed through a polarization controller (PC). The PC is adjusted to produce the optimum polarization for modulation in the SDL MOD-9140 electro-optic modulator (EOM). A 4.8V DC bias is supplied to the EOM DC port to shift modulation to the linear region of the modulator, and a $4V_{PP}$ sinusoidal voltage signal of frequency 1kHz is supplied to the RF port to drive modulation. The modulator output is then connected to the launch fiber for SOA1. Figure 4.4 contains an optical oscilloscope

capture of the modulated signal out of the EOM, showing a 1 kHz sinusoidal optical signal with an extinction ratio of 11.5dB.

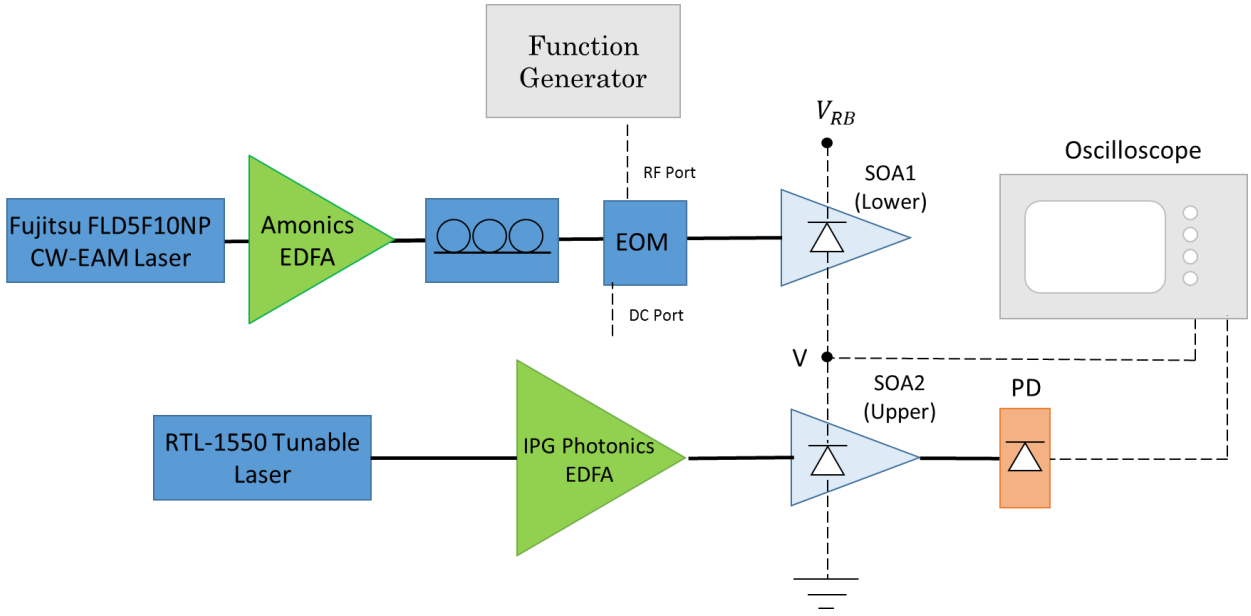


**Figure 4.3: Equipment setup for bistable switching at 1kHz modulation frequency**

Extinction ratio is calculated as:

$$Extinction\ Ratio = 10 \log_{10} \frac{P_{high}}{P_{low}} \tag{4.2}$$

where $P_{high}$ is the maximum optical power of the sinusoidal signal, and $P_{low}$ is the minimum optical power of the signal. $P_{high}$ and $P_{low}$ are measured with the horizontal cursors in Fig. 4.4.

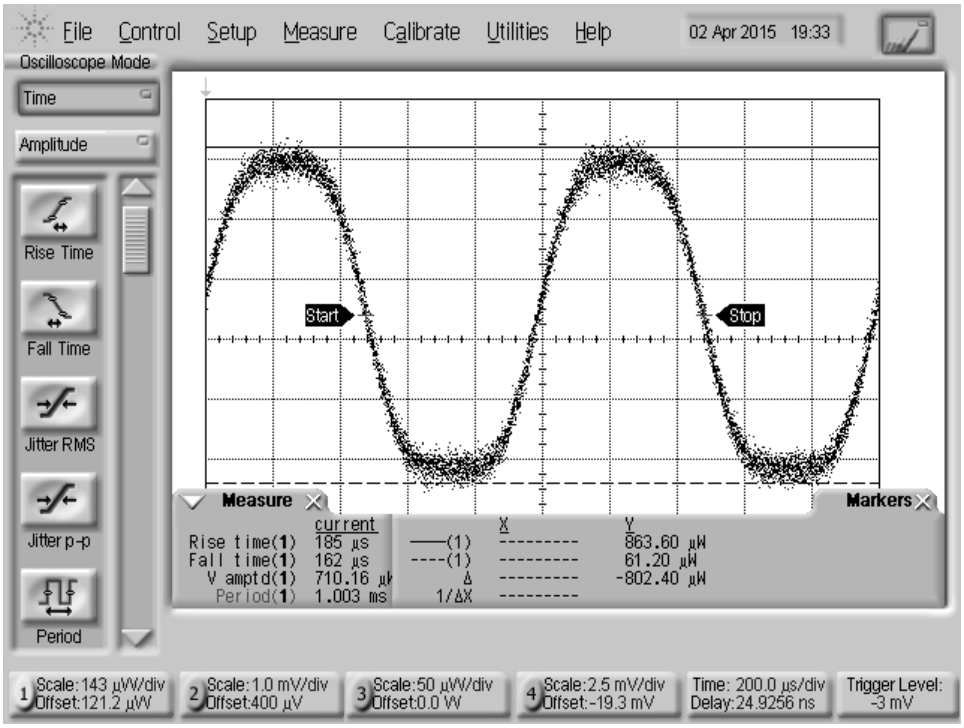


**Figure 4.4: 1kHz sinusoidal optical signal out of the EOM**

The CW optical signal is supplied by the RTL-1550 laser, amplified by an IPG Photonics EAD-500-CL EDFA. The EDFA output is connected to the launch fiber for SOA2. In order to achieve a switching signal that reaches both stable voltage states, the CW signal into SOA2 was set to an optical power of ~8dBm. The power of the optical signal into SOA1 is then adjusted until the voltage, V, is somewhere in between the two stable voltage states by adjusting the drive current of the Amonics EDFA. Once the voltage is in the required region, the modulating voltage signal to the EOM is then turned on. The Amonics EDFA current is once again adjusted until the signal reaches both stable voltage states. Final system operating parameters are listed in Table 4.2 below.

| **Fujitsu FLD5F10NP Laser** | | |
|---|---|---|
| **Parameter** | **Value** | **Uncertainty** |
| I (mA) | 100.0 | ± 0.05 |
| Peak λ (nm) | 1553.9 | ± 0.05 |
| **Amonics AEDFA-C-15B-LCB-R EDFA** | | |
| **Parameter** | **Value** | **Uncertainty** |
| I (mA) | 100 | ± 0.5 |
| Output Power (dBm) | 7.6 | ± 0.05 |
| **SDL EOM 9140** | | |
| **Parameter** | **Value** | **Uncertainty** |
| DC Input (V) | 4.80 | ± 0.005 |
| RF Input (Vpp) | 4.00 | ± 0.005 |
| Peak Output Power (dBm) | 0.6 | ± 0.05 |
| **RTL-1550-10-M Tunable Laser** | | |
| **Parameter** | **Value** | **Uncertainty** |
| I (mA) | 300 | ± 0.5 |
| Peak λ (nm) | 1540 | ± 0.5 |
| **IPG Photonics EAD-500-CL EDFA** | | |
| **Parameter** | **Value** | **Uncertainty** |
| I (mA) | 320 | ± 0.5 |
| Output Power (dBm) | 10.2 | ± 0.05 |

**Table 4.2: System operation parameters for 1 kHz operation when $V_{RB} = 2.000V$**

The switching voltage signals are viewed on an oscilloscope. The switching voltage can be seen in Fig. 4.5, and an x-y plot of the input signal and output voltage signal is included in Fig. 4.6.

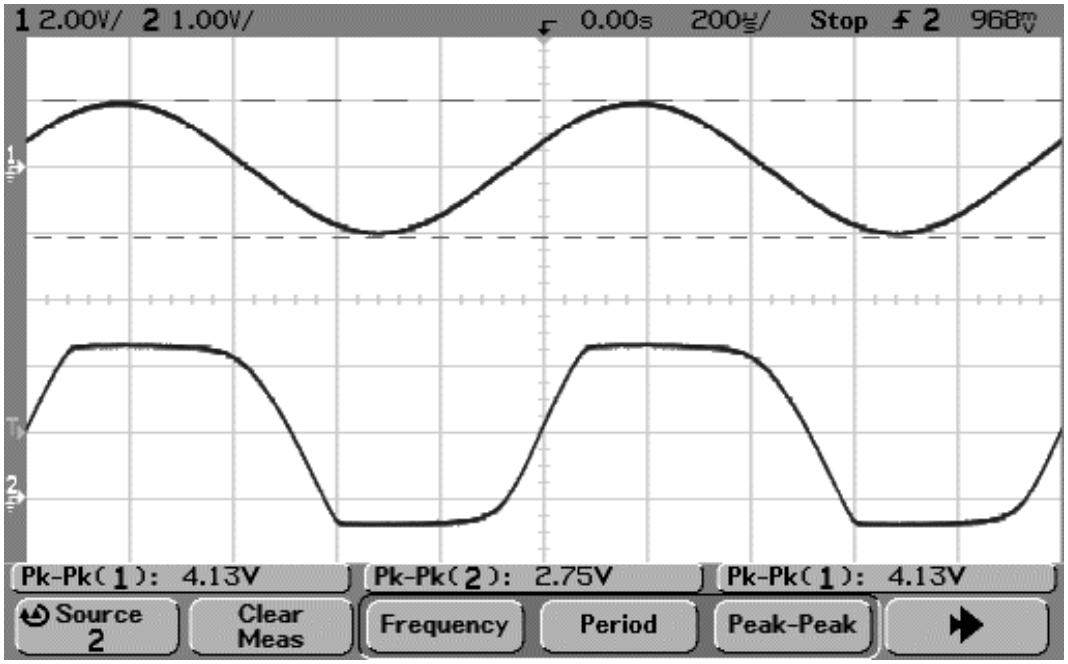


**Figure 4.5: Switching voltage signal V (signal 2) along with voltage signal input to modulator (signal 1), system operating at 1kHz frequency**

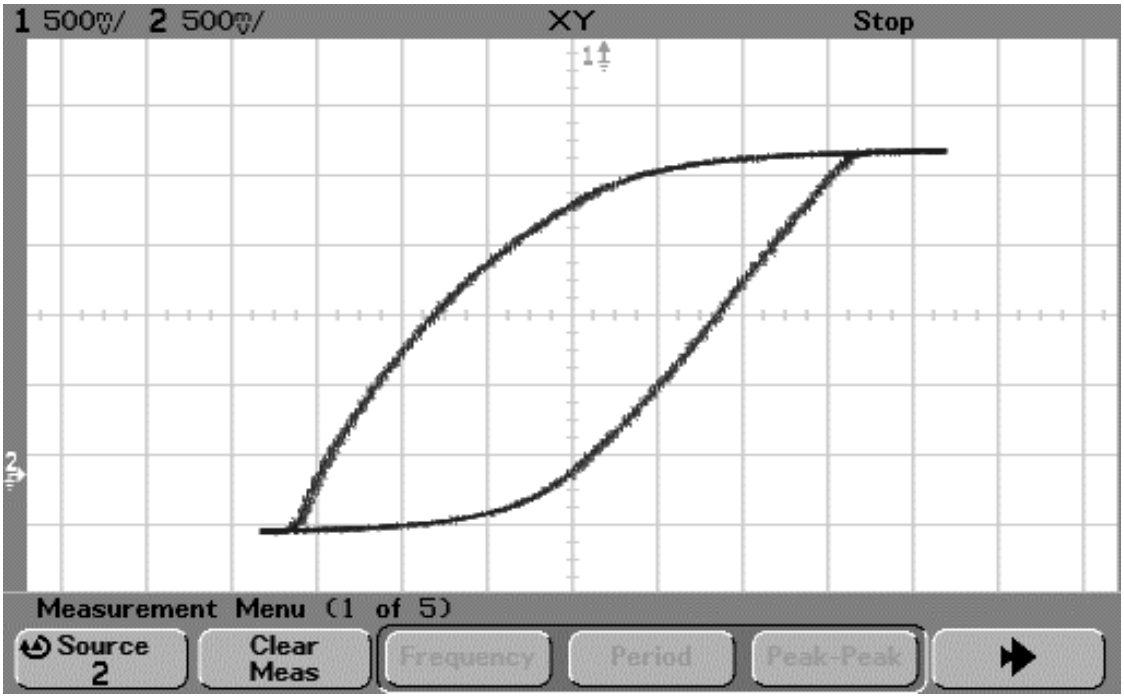


**Figure 4.6: XY plot of input/output signal to the system, showing bistable switching behavior, system operating at 1kHz frequency**

The voltage signal V in Fig. 4.5 exhibits the expected behavior as the signal switches between two stable voltage states. The upper state, a voltage slightly higher than $V_{RB}$, is achieved when the input optical power into SOA1 is greater than the input optical power to SOA2. The lower voltage state, slightly less than zero, is achieved when the input optical power into SOA1 is less than the input optical power to SOA2. This matches the expected system operation outlined in Section 2.4 and in Fig. 2.7.

The x-y plot in Fig. 4.6 proves that the system exhibits the expected electrical bistability described in Chapter 1. Notice that plots shows a hysteresis behavior. When the input modulated optical signal is increasing, the voltage V stays towards the low voltage state, and when the modulated optical signal is decreasing, the voltage V stays towards the high voltage state. This non-inverted behavior also matches the expected behavior described in Section 2.4.

Oscilloscope captures of the voltage across SOA1, as well as x-y hysteresis plot, are included in Fig. 4.7 and Fig. 4.8, respectively. In this case, the voltage response is inverted with respect to the input optical signal to SOA. A high optical input results in a low voltage output, while a low optical input results in a higher voltage output. This matches the expected result, as discussed in Section 2.4.

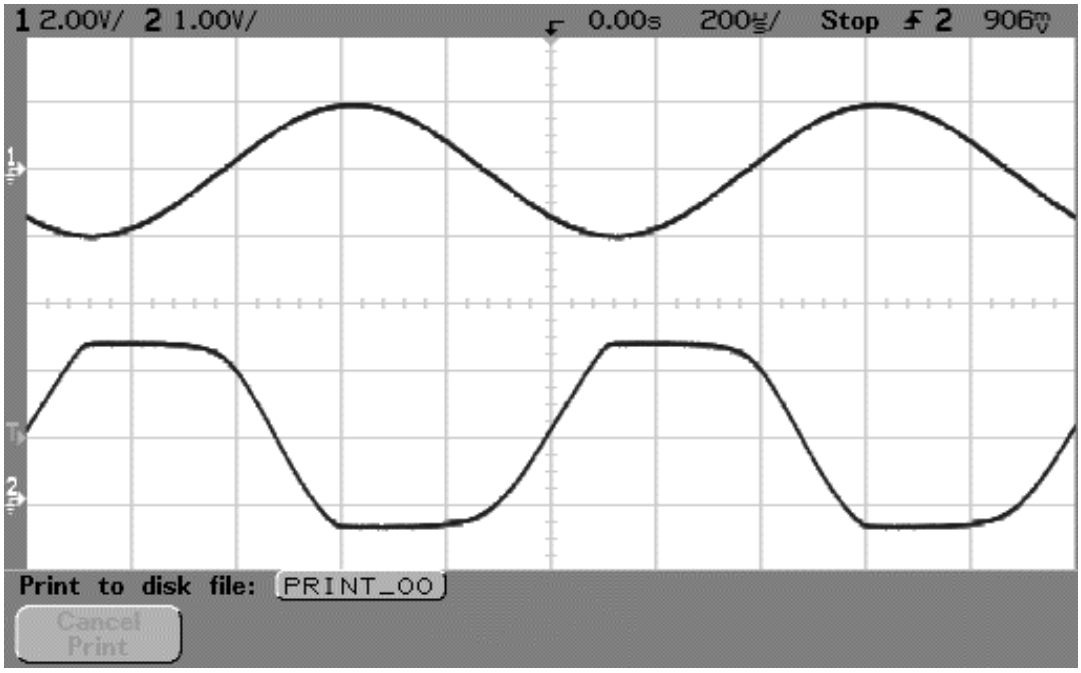


**Figure 4.7: Switching voltage signal across SOA1 (signal 2), plotted along with the voltage input to the EOM (signal 1), system operating at 1kHz frequency**

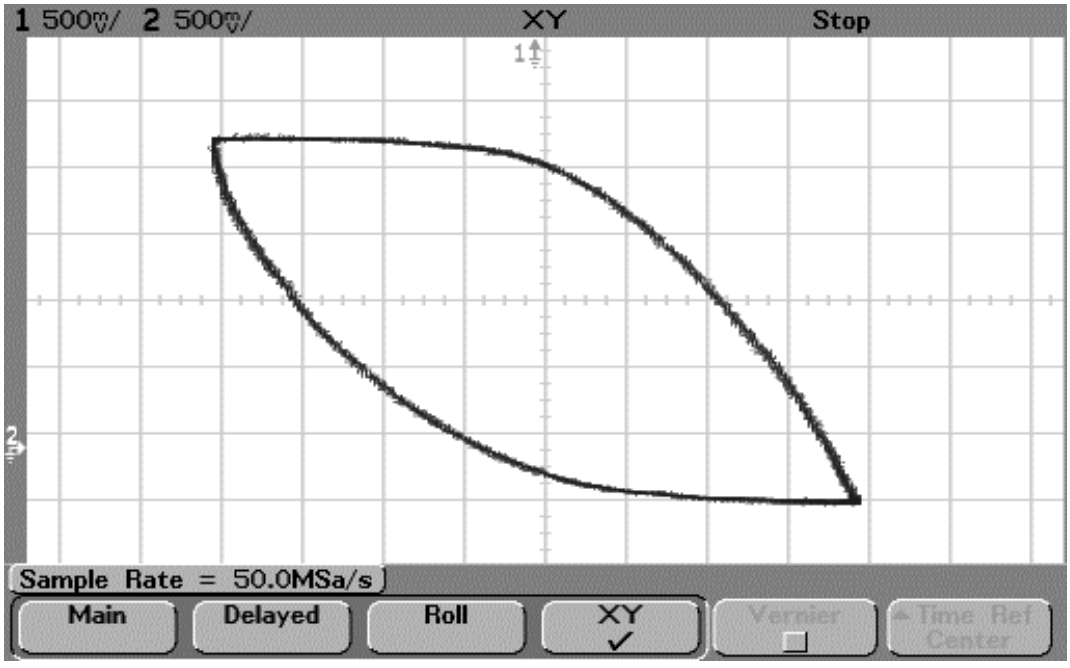


**Figure 4.8: XY Plot of the input/output signals of the system, showing bistable, inverted hysteresis behavior, system operating at 1kHz frequency**

### 4.4 Bistable Switching at Higher Speeds

Once bistable switching operation had been verified at 1 kHz, improvements were necessary to further increase switching speeds. With the system set up as in Fig. 4.3, increasing the modulation frequency into the modulator past 1 kHz resulted in significant degradation of the signal amplitude. To achieve switching speeds beyond 1 kHz the optical power out of each launch fiber had to be increased, the voltage probe was swapped for a high frequency RF voltage probe, and fiber alignment had to be even further optimized.

The equipment setup for switching at higher speeds is illustrated in Fig. 4.9. To achieve higher optical power out of the modulated signal launch fiber, the Fujitsu laser was swapped out with a higher power Alcatel A 1905 LMI diode laser, capable of outputting up to 10 mW power, much higher than the Fujitsu laser's maximum output of just over 2 mW. Additionally, the EOM was connected before the EDFA instead of after, giving an optical signal with a smaller modulation depth but a greater average power. Also the modulated signal was put into SOA2, since it was possible to couple more power into this SOA than into SOA1.

Switching with this setup was first established at 1 kHz, and the frequency was then increased. Each time the frequency was increased, the EDFA drive current was increased and optical alignment had to be fine-tuned to reestablish strong switching behavior. This procedure was repeated up to a frequency of 400 kHz. When modulating at frequencies higher than 400kHz the voltage signal no longer reached its maximum and minimum values, resulting in a signal that was rounded rather than flat on top and bottom. Oscilloscope captures showing the hysteretic bistable voltage switching at frequencies up to 400 kHz are included in Fig. 4.10 to

Fig. 4.19. System parameters for operation at the maximum switching speed can be found in Table 4.3.

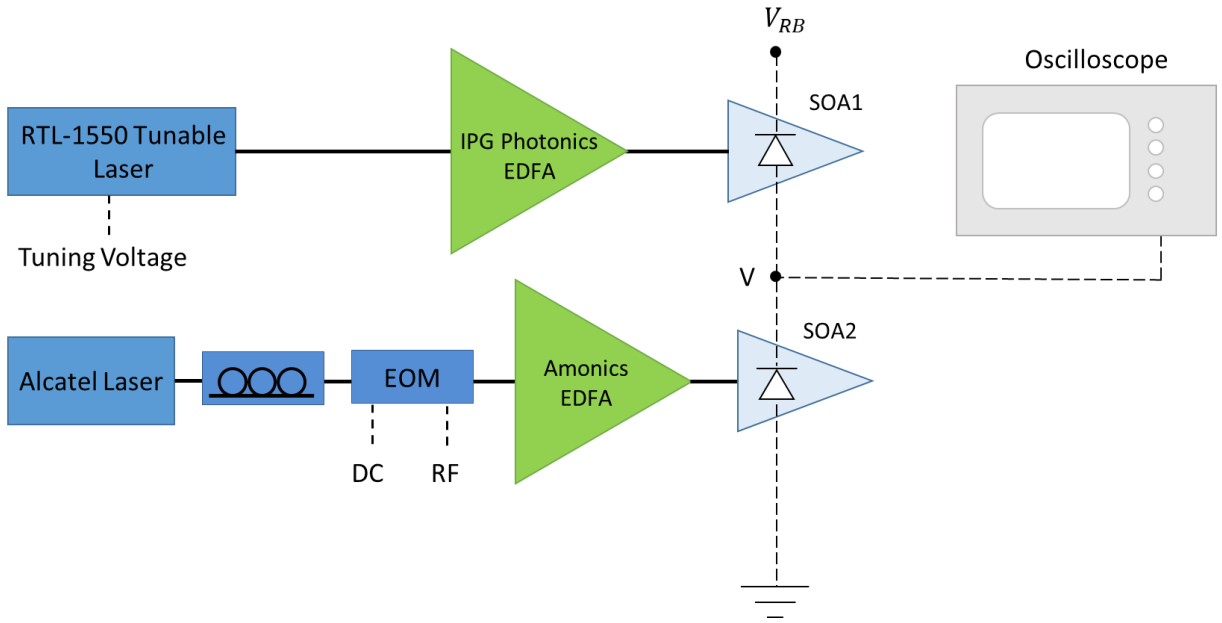


**Figure 4.9: Equipment setup for bistable switching frequencies beyond 1 kHz**

As the modulation frequency increases, the hysteresis windows in the XY plots gradually widen, and the voltage signal becomes more rounded when approaching its maximum and minimum values. The SOAs must generate higher photocurrents to achieve higher switching speeds. The drive current for both lasers and EDFAs had to be increased to their absolute maximum values for the system to operate at a frequency of 400 kHz, so switching beyond this frequency was not possible with this equipment setup. Final system operating parameters are in Table 4.3.

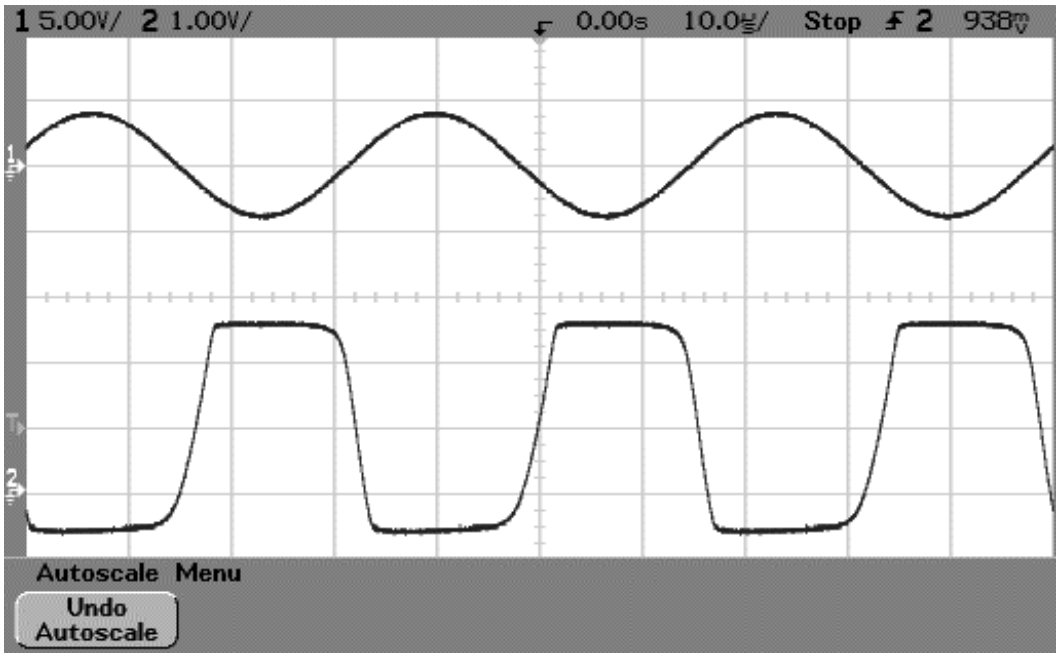


**Figure 4.10: 30 kHz switching voltage V (2), along with the voltage signal into EOM (1)**

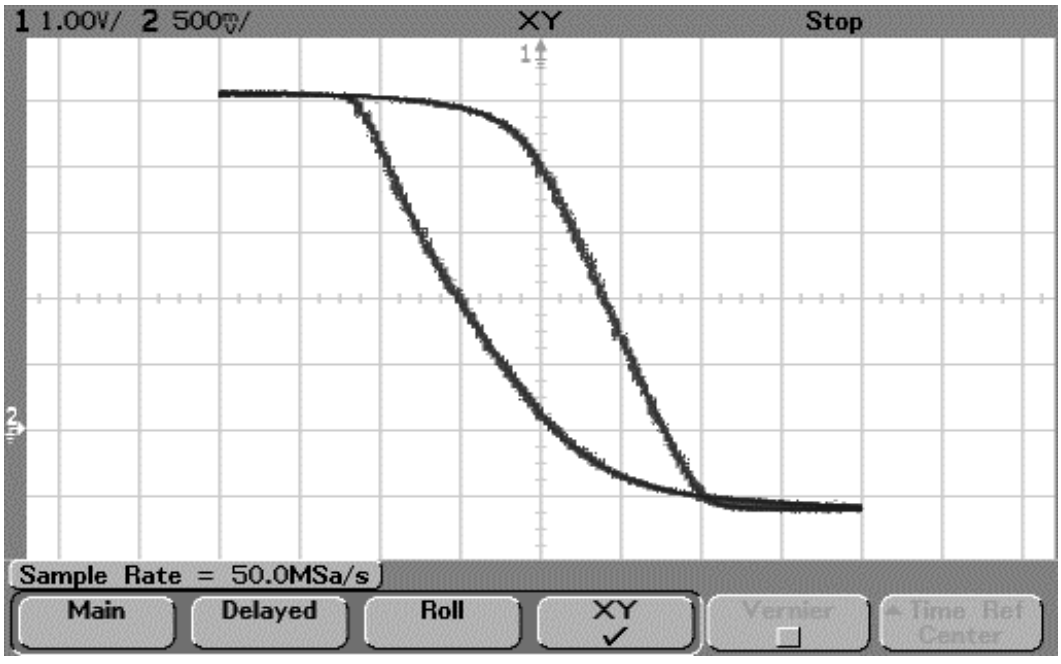


**Figure 4.11: XY plot of the input/output of the system operating at 30 kHz switching speed, showing inverted hysteresis behavior**

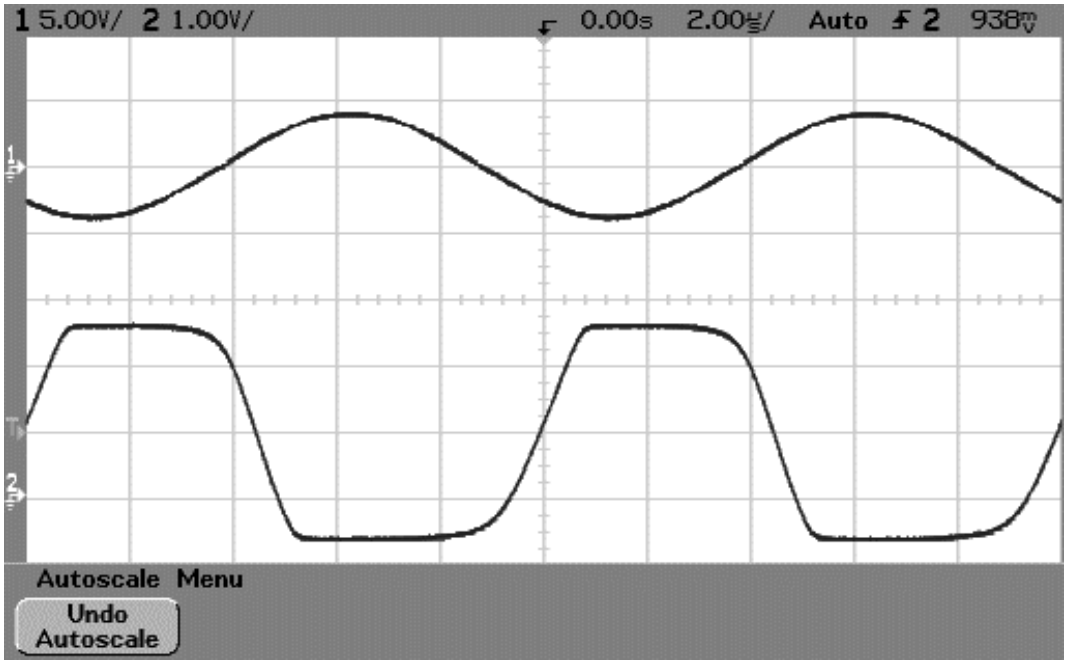


**Figure 4.12: 100 kHz switching voltage V (2), along with the voltage signal into EOM (1)**

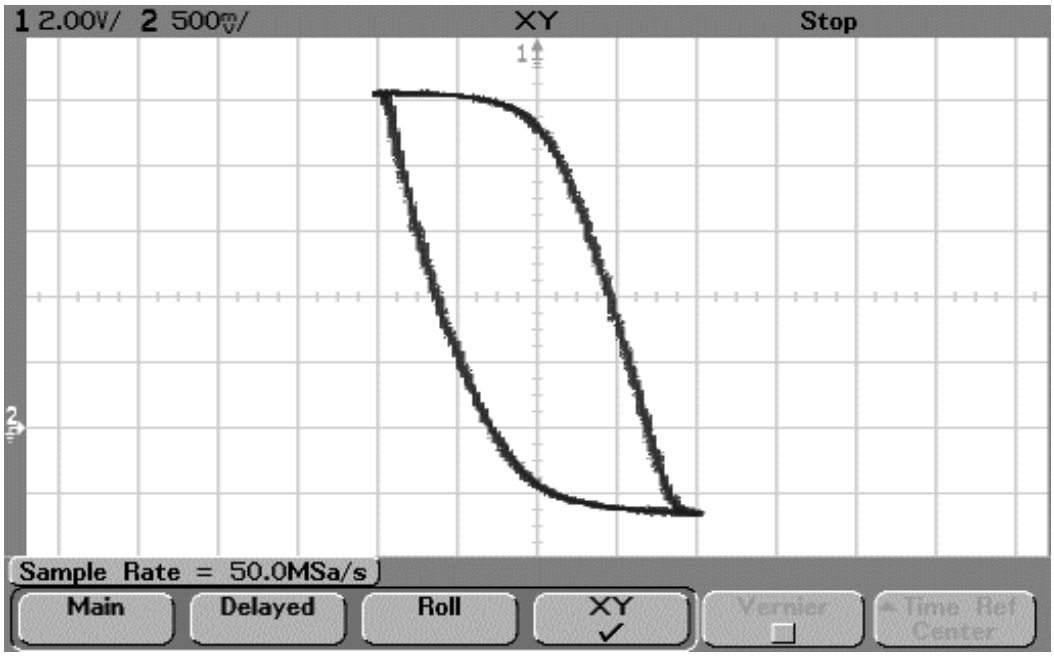


**Figure 4.13: XY plot of the input/output of the system operating at 100 kHz switching speed, showing inverted hysteresis behavior**

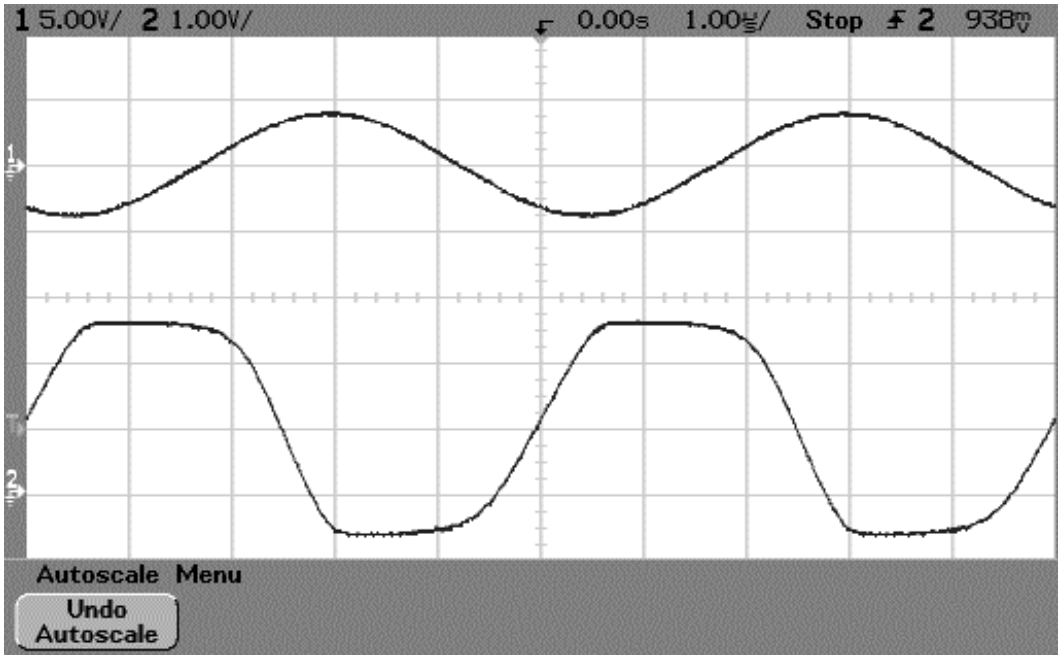


**Figure 4.14: 200 kHz switching voltage V (2), along with the voltage signal into EOM (1)**

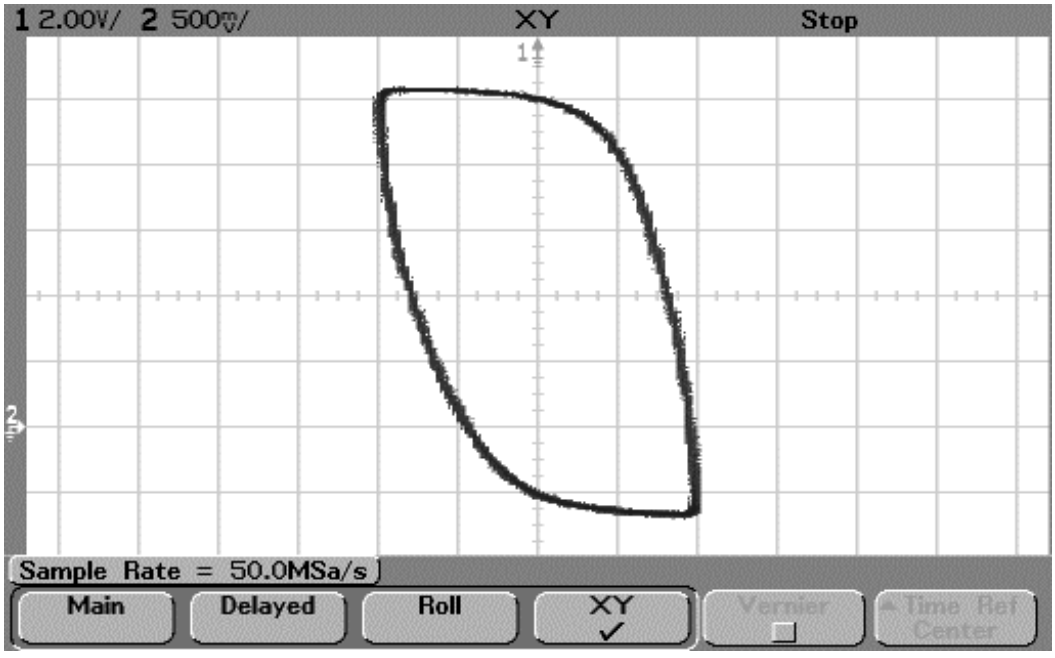


**Figure 4.15: XY plot of the input/output of the system operating at 200 kHz switching speed, showing inverted hysteresis behavior**

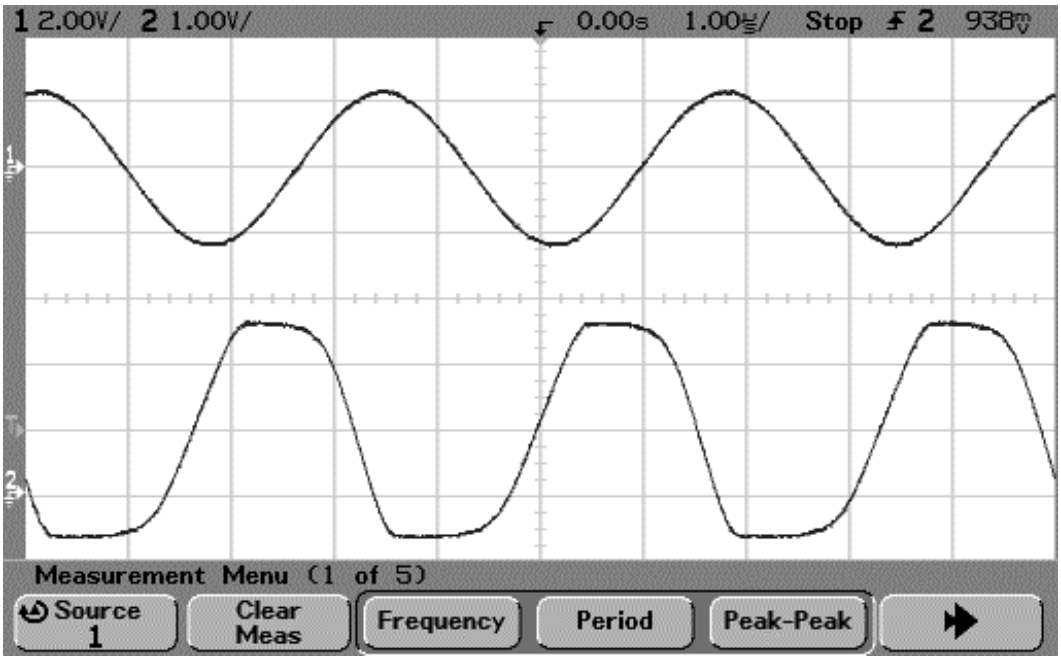


**Figure 4.16: 300 kHz switching voltage V (2), along with the voltage signal into EOM (1)**

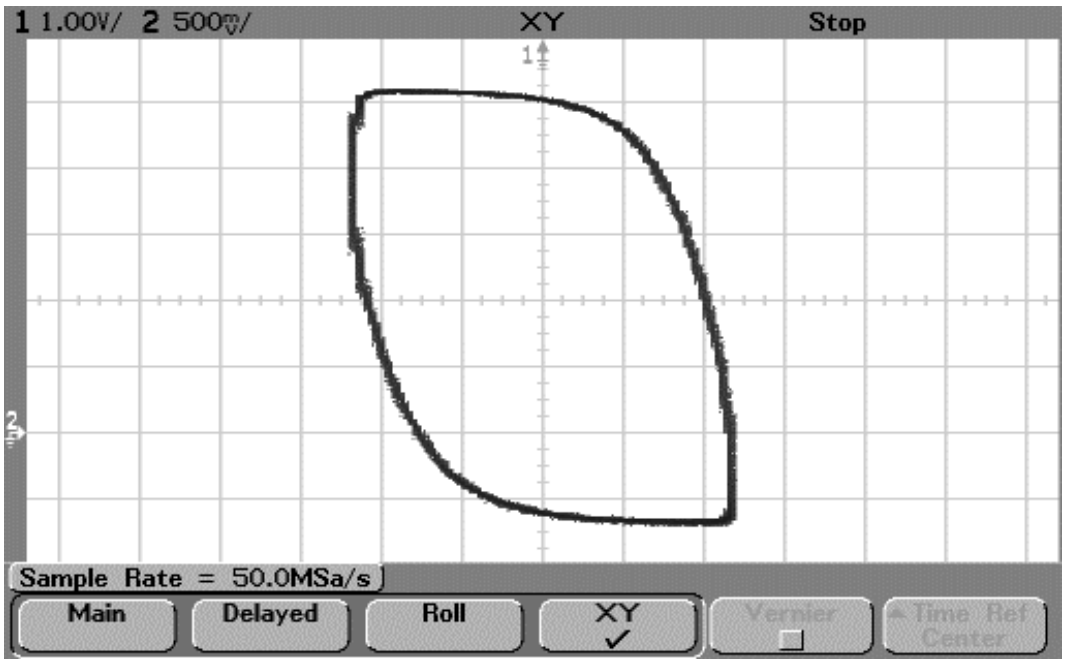


**Figure 4.17: XY plot of the input/output of the system operating at 200 kHz switching speed, showing inverted hysteresis behavior**

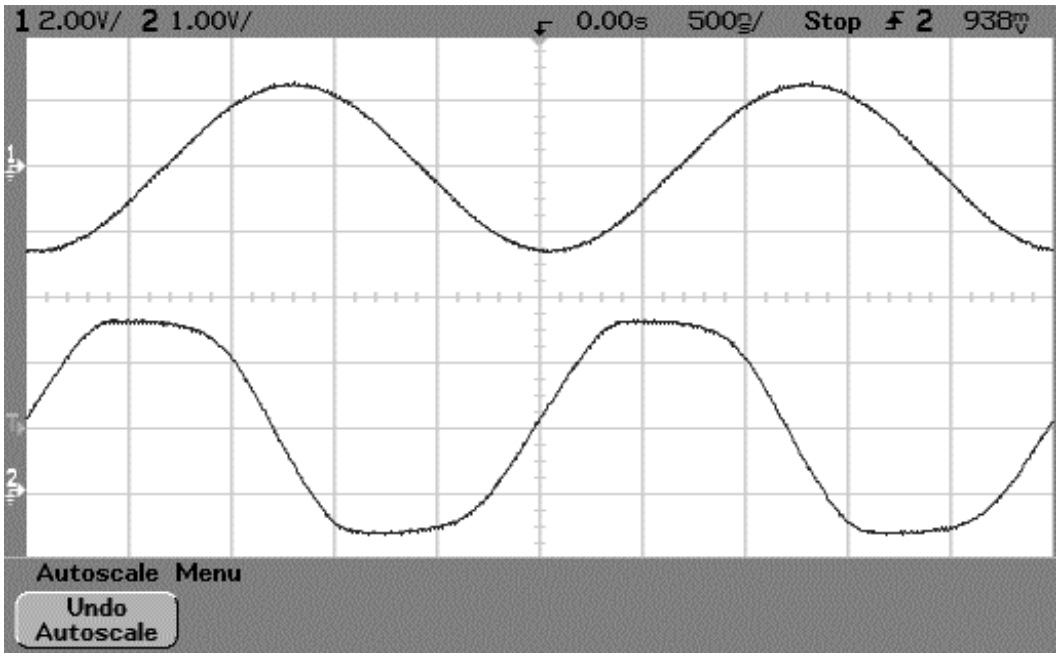


**Figure 4.18: 400 kHz switching voltage V (2), along with the voltage signal into EOM (1). At this frequency, the voltage signal is much more rounded on the edges than at lower frequencies, looking almost like a sinusoidal signal.**

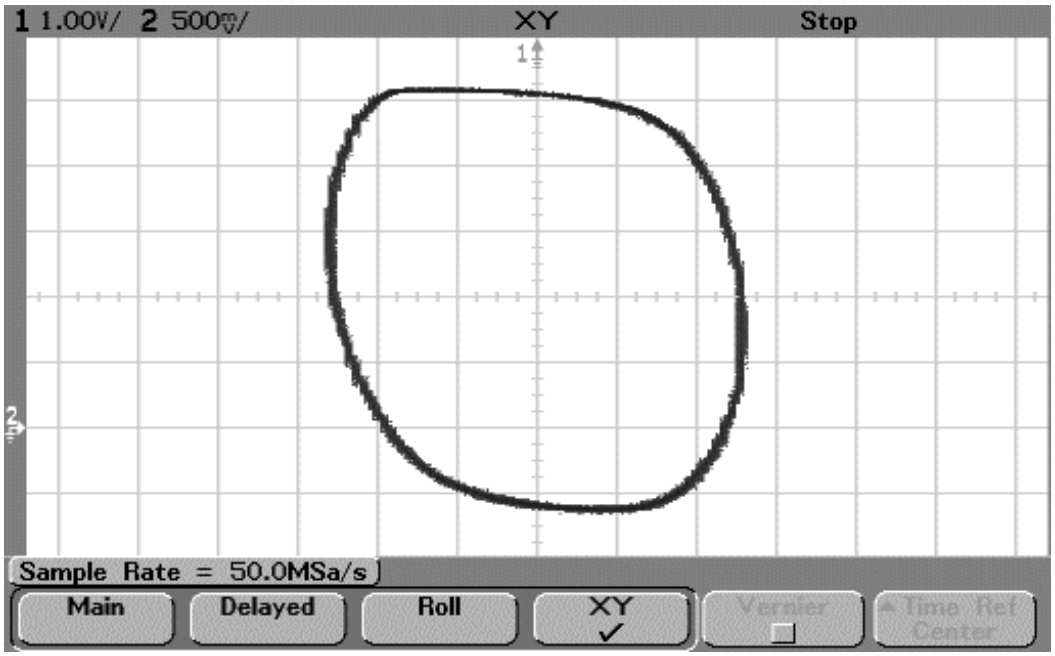


**Figure 4.19: XY plot of the input/output of the system operating at 400 kHz switching speed, showing inverted hysteresis behavior**

| Alcatel A 1905 LMI Laser Diode | | |
|---|---|---|
| **Parameter** | **Value** | **Uncertainty** |
| I (mA) | 50.00 | ± 0.005 |
| Peak λ (nm) | 1551.7 | ± 0.05 |
| **Amonics AEDFA-C-15B-LCB-R EDFA** | | |
| **Parameter** | **Value** | **Uncertainty** |
| I (mA) | 180 | ± 0.5 |
| Peak Output Power (dBm) | 12.3 | ± 0.05 |
| **SDL EOM 9140** | | |
| **Parameter** | **Value** | **Uncertainty** |
| DC Input (V) | 4.80 | ± 0.005 |
| RF Input (Vpp) | 4.00 | ± 0.005 |
| **RTL-1550-10-M Tunable Laser** | | |
| **Parameter** | **Value** | **Uncertainty** |
| I (mA) | 300 | ± 0.5 |
| Peak λ (nm) | 1540 | ± 0.5 |
| **IPG Photonics EAD-500-CL EDFA** | | |
| **Parameter** | **Value** | **Uncertainty** |
| I (mA) | 600 | ± 0.5 |
| Output Power (dBm) | 18.8 | ± 0.05 |

**Table 4.3: System operation parameters for 400 kHz switching operation when $V_{RB} = 2.000V$**

### 4.5 Analysis of System Limitations

As discussed in the previous section, the system requires a greater optical power to operate at higher switching speeds. Considering the model in equation 2.3, the time required for each SOA to charge and discharge is inversely proportional to the difference in optical input powers, $P_{in2} - P_{in1}$. To achieve optimum switching speed, this difference in optical input powers should be maximized, either by stronger modulation of the input optical signal or by improving alignment to the device.

When operating at the maximum speed, the laser diodes and EDFAs are being pushed to their current limits. Also, the EOM is modulating at its maximum capability, so it is not possible to achieve a higher output power or modulation depth using these components. However, it should be possible to couple more light into the system without increasing the power output by the sources.

In Section 3.4 it was demonstrated that coupling light to the SOA's small rectangular waveguide from a bare cleaved single-mode fiber is a very inefficient process. Losses in excess of 18 dB were calculated due to mismatch of mode size and shape. The fundamental mode in the single-mode fiber is very large and radially symmetric, while the fundamental mode for the rectangular waveguide is comparatively very small in size and elliptical in shape – see Fig. 3.11 to Fig. 3.13. In order to minimize the coupling loss, the mode size and shape between optical fiber and rectangular waveguide must be matched as closely as possible.

One possible solution to the problem of mode mismatch is to employ some sort of waveguide taper. Tapered waveguides help to gradually transform the mode shape and size, allowing for a better mode matching between otherwise unlike waveguides. Tapers for mode transformation and more efficient fiber to chip coupling have been successfully demonstrated by fabricating a gradual taper on the end of a semiconductor waveguide [17], citing losses of less than 0.5dB when coupling to a standard single-mode fiber. However such a solution would not be feasible for this project as it would require fabrication of a new device, and this device was fabricated by a third party.

A more realistic solution in this case would be to taper the end of the optical fiber to shrink the mode field diameter of the light leaving the fiber, as illustrated in Fig. 4.20. Tapered optical fibers have been fabricated and experimentally verified to produce MFDs smaller than 1μm,

resulting in coupling losses of just over 1dB when coupling to semiconductor waveguides similar in size to the SOAs presented in this thesis [18]. Tapered optical fibers are also commonly used in commercially available semiconductor waveguides, including SOAs. Fig. 4.21 is a microscope image of a tapered fiber-to-chip coupling system inside of a commercially packaged Covega SOA.

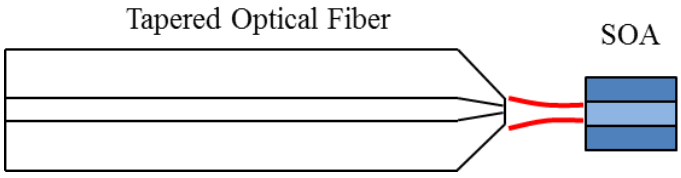


**Figure 4.20: Diagram showing the effect of tapering a single-mode fiber**

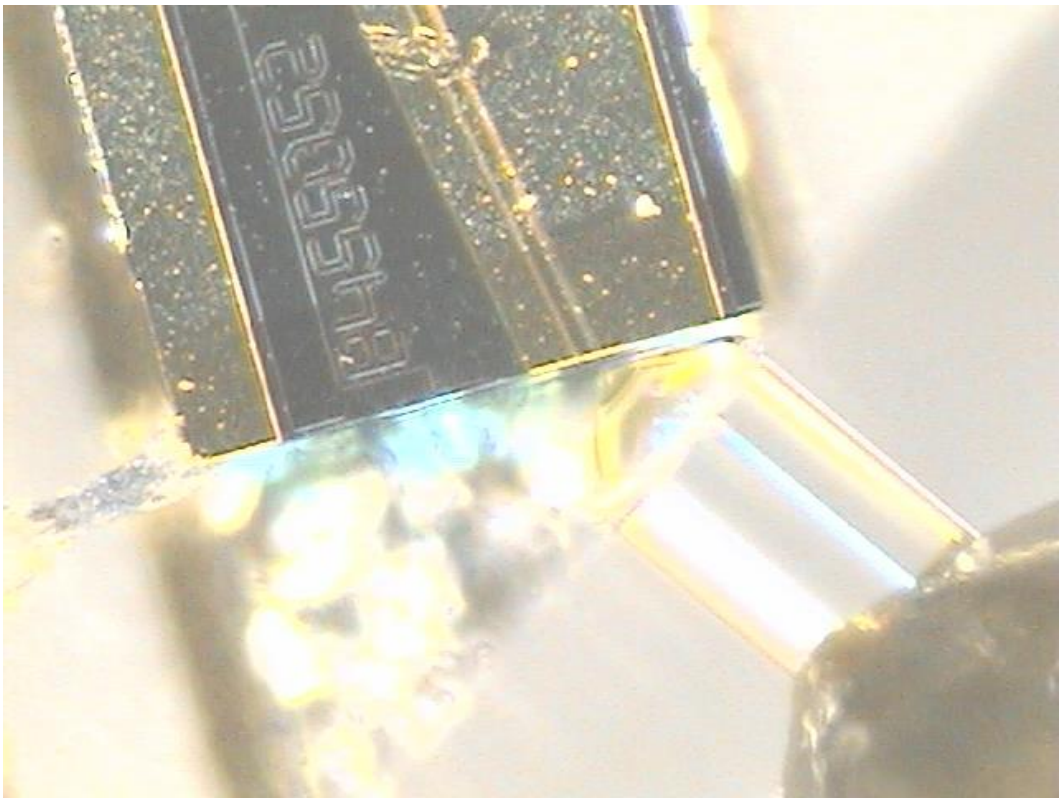

**Figure 4.21: Microscope image of a tapered optical fiber used in a commercially available Covega SOA**

Tapered single-mode fibers are also readily available from optics suppliers. Tapered fibers with MFDs of 2.0 ± 0.5μm were ordered, and were tested in the system as well. Some adjustments had to be made to the alignment system. The Micromanipulator probe holders could not be used since the fibers were not coated in the same 900μm tight buffer coating as the single-mode fibers were. A fiber holder was mounted onto an x-y-z translational stage to align the tapered fibers. Since a larger manipulator had to be used for fiber alignment, only one fiber was able to be aligned to each side of the device. A microscope image of the tapered optical fibers aligned with the SOAs is included in Fig. 4.22.

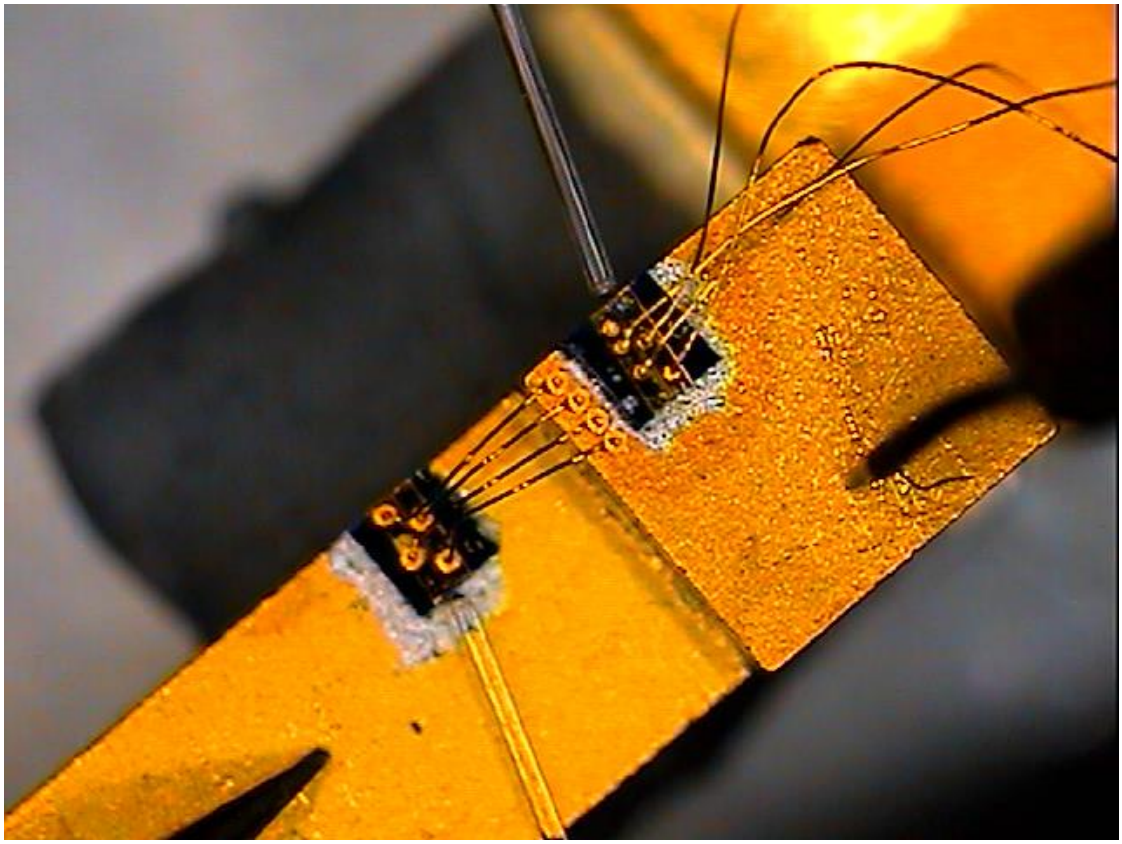

**Figure 4.22: Image of tapered optical fibers aligned with SOAs**

Assuming a fiber MFD of 2.5μm ($\omega_0 = 1.25\mu m$) and rectangular waveguide $1/e$ widths as mentioned in Section 3.4, the total power coupling loss due to mode mismatch as calculated by equations 3.8 and 3.9 is 8.1dB. Fig. 4.23 shows a comparison of the electric field profile cross-sections for this case. The power loss still seems very large, but is actually at least 9dB better than calculated when launching light into the SOA from a 9μm MFD fiber. This loss can be further reduced by tapering the fiber differently in the x and y directions, producing an elliptical spot that will more closely match the shape of the SOA waveguide mode.

Results using the 2μm MFD tapered optical fibers matched the expected results. The maximum spontaneous emission measured when aligning the fibers was consistently 9-10dB higher for both SOAs than when using the 9μm MFD bare single-mode fibers. As seen in Fig. 4.22 however, only two fibers could be aligned at once. This limitation prevents observing the light out of the SOAs. Additionally, the system's alignment stability was significantly decreased due to the fiber being held further from the tip as well as the smaller MFD of the fiber.

Although reducing the MFD of the light entering the SOA waveguide will increase the power coupling efficiency, it will also greatly increase the alignment sensitivity of the system. Since the MFD will be much closer to the size of the waveguide's fundamental mode, misalignment will result in a greater loss in mode profile area overlap. In order to understand this increased sensitivity, compare the effect of a 1μm lateral misalignment for the case of coupling from a 9μm MFD single-mode fiber with the effect in the case of the 2.5μm MFD tapered fiber. In both cases, the electric field of the fundamental mode can be represented by a Gaussian profile, misaligned by 1μm in the x-direction with respect to the center of the rectangular waveguide.

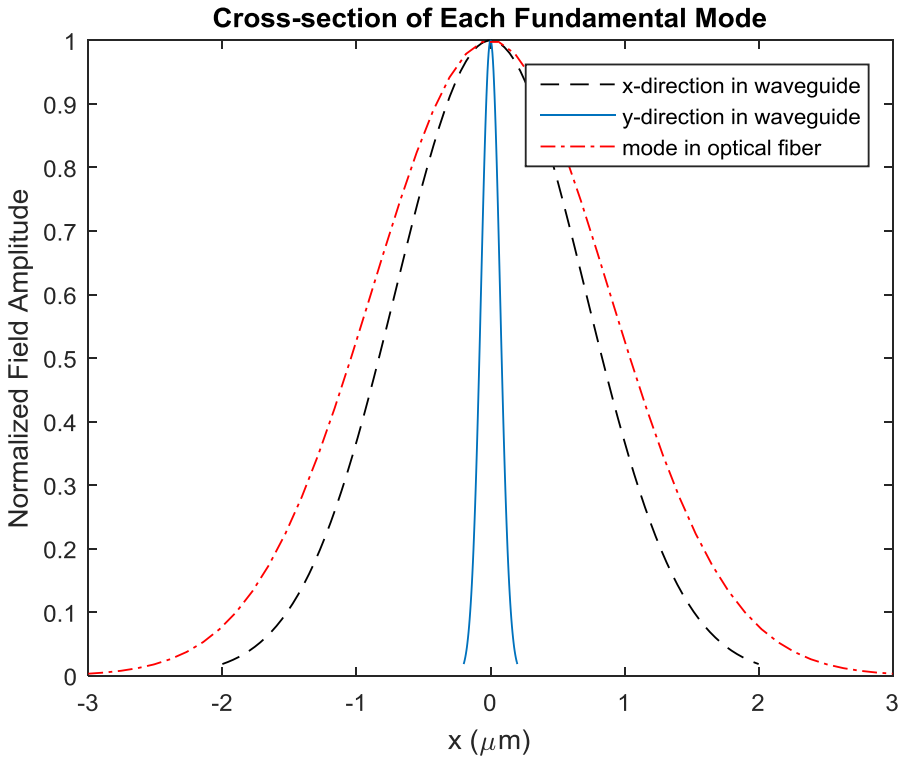


**Figure 4.23: Mode cross-sections for both directions in the rectangular waveguide and in optical fiber with a MFD of 2.5µm**

The normalized field profile for the single-mode fiber is represented by equation 4.3, and by equation 4.4 for the tapered fiber.

$$E_{SMF} = e^{-\frac{((x-1\mu m)^2+y^2)}{(4.5\mu m)^2}} \tag{4.3}$$

$$E_{taper} = e^{-\frac{((x-1\mu m)^2+y^2)}{(1.25\mu m)^2}} \tag{4.4}$$

The field profiles for the fundamental mode in the waveguide will remain the same as in Section 3.4. Taking the square of the overlap integral between the field in the fiber and the waveguide will calculate the power coupling efficiency. This is done for the single-mode fiber in equation 4.5, and for the tapered fiber in equation 4.6.

$$\eta_{SMF} = \left( \frac{\iint_{-\infty}^{\infty} \left| e^{-\frac{((x-1\mu m)^2+y^2)}{(4.5\mu m)^2}} \right| \left| e^{-\left(\frac{x^2}{(1\mu m)^2}+\frac{y^2}{(0.1\mu m)^2}\right)} \right| dx\, dy}{\sqrt{\iint_{-\infty}^{\infty} \left| e^{-\frac{((x-1\mu m)^2+y^2)}{(4.5\mu m)^2}} \right|^2 dx\, dy \iint_{-\infty}^{\infty} \left| e^{-\frac{(x^2+y^2)}{(1\mu m)^2+(0.1\mu m)^2}} \right|^2 dx\, dy}} \right)^2 \quad (4.5)$$

$$\eta_{taper} = \left( \frac{\iint_{-\infty}^{\infty} \left| e^{-\frac{((x-1\mu m)^2+y^2)}{(1.25\mu m)^2}} \right| \left| e^{-\left(\frac{x^2}{(1\mu m)^2}+\frac{y^2}{(0.1\mu m)^2}\right)} \right| dx\, dy}{\sqrt{\iint_{-\infty}^{\infty} \left| e^{-\frac{((x-1\mu m)^2+y^2)}{(1.25\mu m)^2}} \right|^2 dx\, dy \iint_{-\infty}^{\infty} \left| e^{-\frac{(x^2+y^2)}{(1\mu m)^2+(0.1\mu m)^2}} \right|^2 dx\, dy}} \right)^2 \quad (4.6)$$

Using each result in equation 3.9 gives power coupling losses of $L_{SMF} = 17.7dB$, while $L_{taper} = 11.5dB$. Comparing the power coupling loss for the single-mode fiber to the loss calculated in Section 3.4 shows that this 1μm misalignment added about 0.4dB of loss. When the tapered fiber is used, comparing the power coupling losses with and without this 1μm misalignment shows that the same amount of misalignment adds a loss of 3.4dB. This shows that reducing the mode field diameter of the optical fiber will also greatly increase the system loss due to misalignment.

Figure 4.24 demonstrates the effect of this same misalignment on the mode profile area overlap for both scenarios. Comparing the cross-sections for the 9μm MFD fiber with the cross-sections in the case of the tapered fiber, it can be seen that the misalignment will cause a much greater change in mode profile area overlap for the tapered fiber. This shows the reason for the greater power loss given the same misalignment. Additionally, plots showing the total power coupling loss as a function of lateral misalignment are included in Fig. 4.25.

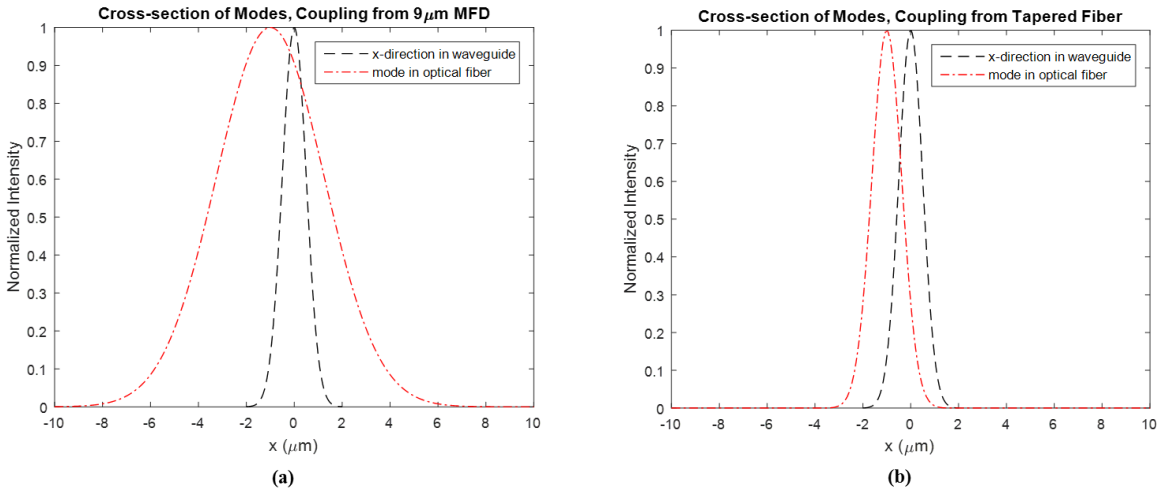


**Figure 4.24: Mode overlap cross-sections showing misalignment for a) coupling from a bare single-mode fiber and b) coupling from a tapered fiber**

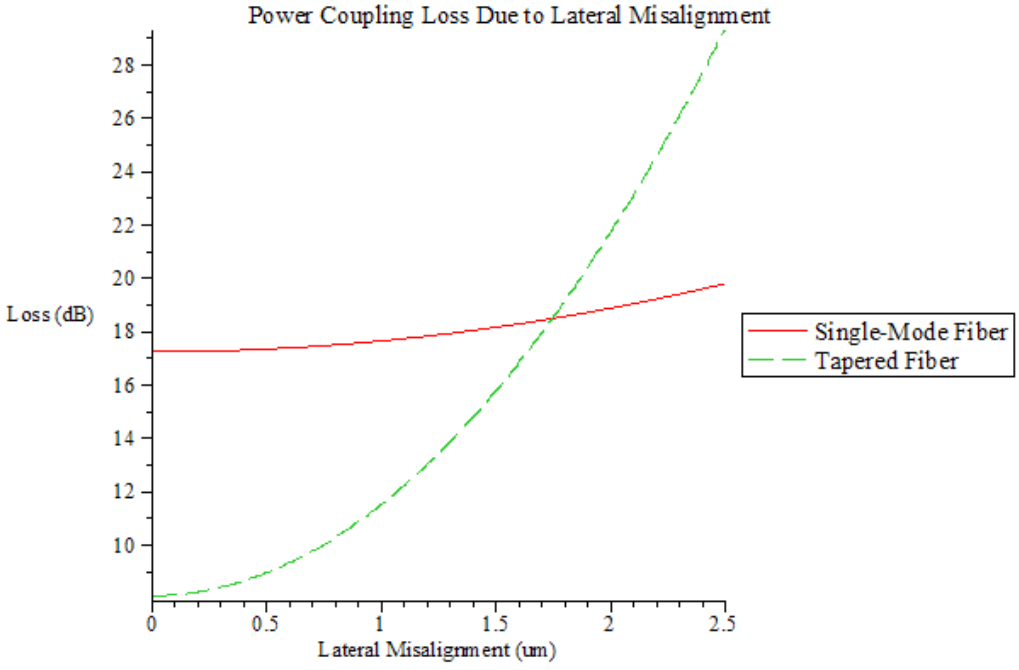


**Figure 4.25: Power coupling loss for single-mode and tapered fibers, plotted as a function of lateral misalignmet distance**

If tapered optical fibers are to be successfully used for coupling light into and out of the SOAs, an alignment system that is more stable than the one presented in this thesis will be necessary to prevent substantial power coupling issues. The system presented here has the tapered fibers held far from the tip and brought close to the SOAs. Since the fibers are suspended in the air, they tend to sway up and down due to air currents or any movement in the system. To prevent this, it is recommended that the alignment system have the fibers aligned and cemented in place to prevent movement of the optical fiber with respect to the SOAs. Fig. 4.26 shows the inside of a packaged commercial SOA waveguide with its fiber alignment system. For comparison, a picture showing the length of fiber suspended in air wen using the tapered fibers is included in Fig. 4.27.

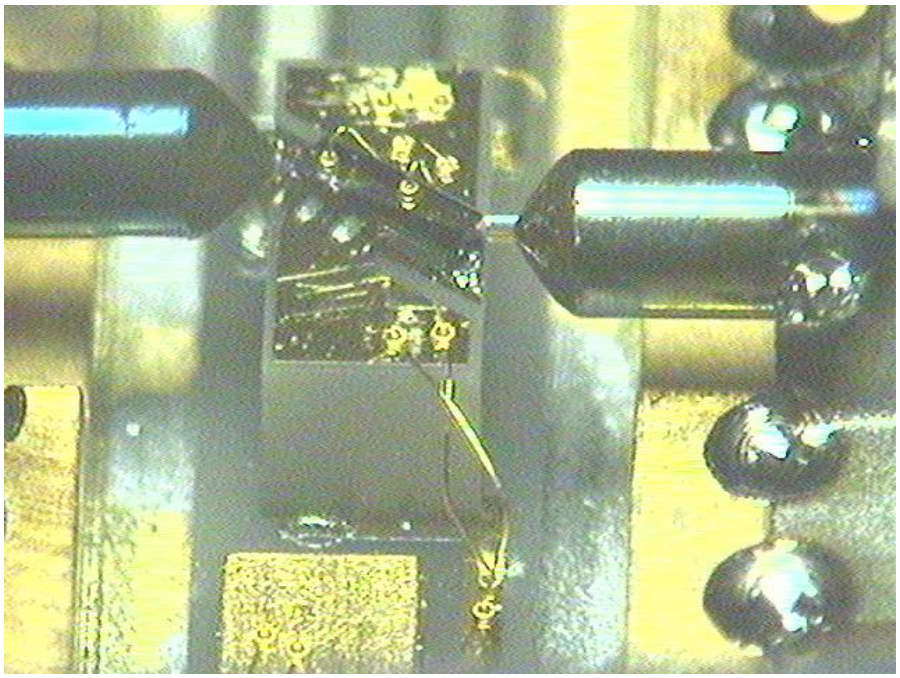

**Figure 4.26: Microscope image of the fiber alignment system inside of a commercially packaged SOA**

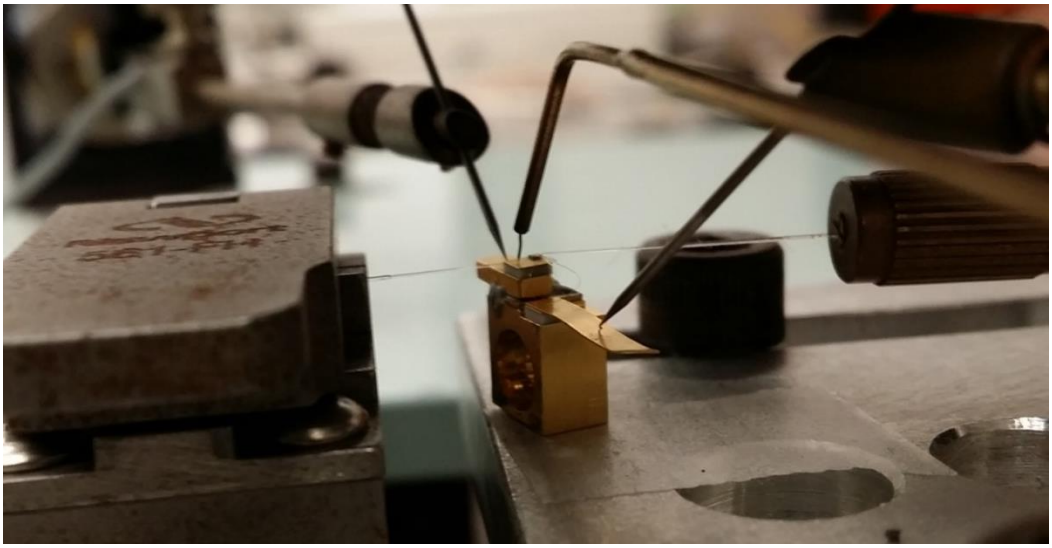

**Figure 4.27: Tapered optical fibers aligned with the SOA device, showing the length of fiber suspended in air that is necessary to accommodate the tapered fibers in this system**

# 5. CONCLUSIONS AND FUTURE WORK

A bistable photonic switch using symmetrically coupled SOAs integrated onto a single device was physically prepared, characterized, and experimentally tested. Bistability was achieved up to a switching frequency of 400 kHz. The system shows electrical bistability with simultaneous inverted and non-inverted hysteresis behavior, resulting in a bistable optical output due to QCSE.

For a switching voltage of 2.000V, the device was demonstrated to produce more than 4dB of optical modulation due to QCSE at a wavelength of 1540 nm. While electro-absorption modulation of light by QCSE is demonstrated in Section 4.2, it was not possible with the coupling system presented to obtain sufficient optical power through the SOA to break the noise floor of the oscilloscope due to coupling losses discussed in Section 3.4. As a result, optical switching could not be observed in real-time.

Device switching performance is significantly hindered by the amount of power that can be coupled into each SOA. The coupled SOA device has the potential to operate at much higher speeds than were achieved in this thesis. Diode capacitance was experimentally measured to be 13.10fF in Section 3.4, suggesting that the device can operate up to frequencies in the gigahertz range [1].

Significant power is lost due to coupling and reflection losses between the large MFD single-mode fiber and the relatively small rectangular waveguides in the SOAs, resulting in the diode capacitances discharging much slower. Using the measured total capacitance, a reverse bias voltage of 2.000V, a realistic responsivity of about 0.3 [8], and just 1mW difference between the power in each SOA, the theoretical maximum switching time is 175ps according to the model in equation 2.3. This corresponds to a maximum obtainable switching frequency of just over 5 GHz.

For operation at 400 kHz, system sources and amplifiers must operate at their absolute maximum outputs, and optimum fiber alignment is necessary to achieve sufficient power coupling to the SOAs. To increase switching speeds beyond 400 kHz it will be necessary to improve the power coupling efficiency as well as increase the modulation of the light into the SOA.

In Section 4.5 it was recommended that tapered optical fibers be used for this system due to their smaller MFD which would more closely match the mode size of the fundamental mode in the SOA waveguide, resulting in lower power coupling loss. Tapered optical fibers were tested in this system and were indeed able to improve coupling to/from the SOAs by up to 10dB. However while the tapered fibers with smaller MFD help improve coupling efficiency, they also greatly increase the system's alignment instability.

Moving forward, it is strongly recommended that any future coupled SOA devices be fabricated and mounted such that a much more stable fiber alignment system can be implemented. Due to the orientation and spacing of the waveguides on the device presented in this thesis, the fibers must be held further from their tip, causing them to be suspended in air and free to move with respect to the waveguide. It is also imperative that a more sophisticated alignment system be constructed for these SOAs to be properly used with tapered optical fibers, while mitigating alignment sensitivity.

## LIST OF REFERENCES

[1] M. Gehl, P. Costanzo-Caso, S. Granieri, A. Siahmakoun, "Optical Bistable Switching with Symmetrically Configured SOAs in Reverse Bias," *Microwave and Opt. Tech. Lett.*, **52**, 2753-2759 (2010).

[2] S. Diez, R. Ludwig, H.G. Weber, "Gain-transparent SOA-switch for High-bitrate OTDM Add/Drop Multiplexing," *Photonics Tech. Lett. IEEE*, **11**, 60-62 (1999).

[3] H. Onaka, Y. Aoki, K. Sone, G. Nakagawa, et. al., "WDM Optical Packet Interconnection using Multi-Gate SOA Switch Architecture for Peta-Flops Ultra-High-Performance Computing Systems," *Optical Communications*, 2006, 1-2 (2006).

[4] B. E. A. Saleh, M. C. Teich, *Fundamentals of Photonics*, Second Edition, Hoboken, NJ: John Wiley & Sons, Inc., 2007.

[5] D. A. B. Miller, "*Optical Physics of Quantum Wells,"* Stanford Electrical, 1994.

[6] D. A. B. Miller, D. S. Chemela, T. C. Damen, T. H. Wood, C.A. Burrus Jr., A. C. Gossard, and W. Wiegman, "The Quantum Well Self-electrooptic Effect Device: Optoelectronic Bistability and Oscillation, and Self-Linearized Modulation," *IEEE J. Quantum Electron.*, QE-21, 1462-1476 (1985).

[7] A. L. Lentine, H. S. Hinton, D. A. B. Miller, J. E. Henry, J. E. Cunningham, L. M. F. Chirovsky, "Symmetric Self-Electrooptic Effect Device: Optical Set-Reset Latch, Differential Logic Gate, and Differential Modulator/Detector," *IEEE J. Quantum Electron.*, QE-25, 1928-1936 (1989).

[8] D. A. B. Miller, D. S. Chemla, T. C. Damen, A. C. Gossard, W. Wiegmann, T.H. Wood and C. A. Burris, "Novel hybrid optically bistable switch: The quantum well self-electro-optic effect device", *Appl. Phys. Lett.*, 45 (1), 13-15 (1 July 1984).

[9] G. Harman, *Wire Bonding in Microelectronics*, Third Edition, The McGraw-Hill Companies, Inc., 2010, pp. 2-6.

[10] R. G. Hunsperger, A. Yariv, and A. Lee, "Parallel end-butt coupling for optical integrated circuits," *Applied Optics*, Vol. 16, No. 4, April 1977

[11] G. Keiser, *Optical Fiber Communications*, Fourth Edition, McGraw-Hill, pp. 223-229, 2011.

[12] T. C. Chu and A. R. McCormick, "Measurement of loss due to offset, end separation and angular misalignment in graded index fibers excited by incoherent source," *Bell Sys. Tech. J.*, vol. 57, pp. 595-602, Mar. 1978.

[13] D. L. Lee, *Electromagnetic Principles of Integrated Optics*, John Wiley & Sons Ltd., 1986.

[14] G. T. Reed and A. P. Knights, *Silicon Photonics: An Introduction*, John Wiley & Sons Ltd., 1st edition, 2004.

[15] F. L. Pedrotti, L. S. Pedrotti, L. M. Pedrotti, *Introduction to Optics*, Pearson Education, Inc., 3rd edition, 2007.

[16] S. R. Selmic, T. M. Chou, J. Sih, J. B. Kirk, A. Mantie, J. K. Butler, D. Bour, and G. A. Evans, "Design and Characterization of 1.3-μm AlGaInAs-InP Multiple-Quantum-Well Lasers", *IEEE Journal on Selected Topics in Quantum Electronics*, Vol. 7, No. 2, March/April 2001.

[17] V. R. Almeida, R. R. Panepucci, and M. Lipson, "Nanotaper for compact mode conversion", *Optics Letters*, Vol. 28, No. 15, August 1, 2003.

[18] T. Alder, A. Stöhr, R. Heinzelmann, and D. Jäger, "High-Efficiency Fiber-to-Chip Coupling Using Low-Loss Tapered Signle-Mode Fiber", *IEEE Photonics Letters*, Vol. 12, No. 8, August 2000.

[19] S. Weisser, I. Esquivias, P. J. Tasker, J. D. Ralston, and J. Rosenzweig, "Impedance, Modulation Response, and Equivalent Circuit of Ultra-High-Speed $In_{0.35}Ga_{0.65}As/GaAs$ MQW Lasers with p-Doping", IEEE Photonics Technology, Vol. 6, No. 7, July 1994.

[20] W. S. C. Chang, RF Photonic Technology in Optical Fiber Links, Cambridge University Press, 2002.

## Appendix A: SOA Transmission Measurements for QCSE

$$\lambda = 1530\text{nm}$$

| VRB | Pmeas1 (dBm) | Pmeas2 (dBm) | Pmeas3 (dBm) | Average | Standard Error (±) | Transmission (dB) |
|---|---|---|---|---|---|---|
| 0.000 | -49.4 | -50.2 | -49.6 | -49.73 | 0.240 | -57.43 |
| 0.250 | -50.3 | -50.3 | -49.8 | -50.13 | 0.167 | -57.83 |
| 0.500 | -50.6 | -50.4 | -50.0 | -50.33 | 0.176 | -58.03 |
| 0.750 | -50.8 | -50.8 | -50.2 | -50.60 | 0.200 | -58.30 |
| 1.000 | -51.4 | -51.2 | -50.5 | -51.03 | 0.273 | -58.73 |
| 1.500 | -52.2 | -51.8 | -51.4 | -51.80 | 0.231 | -59.50 |
| 2.000 | -52.6 | -52.6 | -52.3 | -52.50 | 0.100 | -60.20 |

**Table A.1: Transmission data collected for different bias voltages at λ = 1530nm**

$$\lambda = 1535\text{nm}$$

| VRB | Pmeas1 (dBm) | Pmeas2 (dBm) | Pmeas3 (dBm) | Average | Standard Error (±) | Transmission (dB) |
|---|---|---|---|---|---|---|
| 0.000 | -51.2 | -51.6 | -52.0 | -51.60 | 0.231 | -59.71 |
| 0.250 | -50.9 | -51.4 | -51.9 | -51.40 | 0.289 | -59.10 |
| 0.500 | -50.8 | -51.2 | -51.7 | -51.23 | 0.260 | -58.93 |
| 0.750 | -50.7 | -51.1 | -51.5 | -51.10 | 0.231 | -58.80 |
| 1.000 | -50.6 | -50.9 | -51.3 | -50.93 | 0.203 | -58.63 |
| 1.500 | -50.5 | -50.9 | -51.1 | -50.83 | 0.176 | -58.53 |
| 2.000 | -50.8 | -51.1 | -51.5 | -51.13 | 0.203 | -58.83 |

**Table A.2: Transmission data collected for different bias voltages at λ = 1535nm**

$\lambda = 1540nm$

| VRB | Pmeas1 (dBm) | Pmeas2 (dBm) | Pmeas3 (dBm) | Average | Standard Error (±) | Transmission (dB) |
|---|---|---|---|---|---|---|
| 0.000 | -57.7 | -58.1 | -58.7 | -58.17 | 0.291 | -64.50 |
| 0.250 | -57.6 | -57.8 | -58.3 | -57.90 | 0.208 | -64.23 |
| 0.500 | -56.9 | -57.1 | -57.7 | -57.23 | 0.240 | -63.57 |
| 0.750 | -56.3 | -56.5 | -57.2 | -56.67 | 0.273 | -63.00 |
| 1.000 | -55.6 | -55.8 | -56.5 | -55.97 | 0.273 | -62.30 |
| 1.500 | -54.6 | -54.9 | -55.3 | -54.93 | 0.203 | -61.27 |
| 2.000 | -54.1 | -54 | -54.5 | -54.20 | 0.153 | -60.53 |

**Table A.3: Transmission data collected for different bias voltages at λ = 1540nm**

$\lambda = 1545nm$

| VRB | Pmeas1 (dBm) | Pmeas2 (dBm) | Pmeas3 (dBm) | Average | Standard Error (±) | Transmission (dB) |
|---|---|---|---|---|---|---|
| 0.000 | -53.2 | -54 | -55.2 | -54.13 | 0.581 | -61.39 |
| 0.250 | -53.6 | -54.6 | -55.5 | -54.57 | 0.549 | -61.83 |
| 0.500 | -54 | -55.1 | -55.9 | -55.00 | 0.551 | -62.26 |
| 0.750 | -54.2 | -55.7 | -56.4 | -55.43 | 0.649 | -62.69 |
| 1.000 | -54.9 | -56.3 | -56.8 | -56.00 | 0.569 | -63.26 |
| 1.500 | -55.7 | -57.4 | -57.9 | -57.00 | 0.666 | -64.26 |
| 2.000 | -56.1 | -57.8 | -58.4 | -57.43 | 0.689 | -64.69 |

**Table A.4: Transmission data collected for different bias voltages at λ = 1545nm**

$\lambda = 1550nm$

| VRB | Pmeas1 (dBm) | Pmeas2 (dBm) | Pmeas3 (dBm) | Average | Standard Error (±) | Transmission (dB) |
|---|---|---|---|---|---|---|
| 0.000 | -47.9 | -47.8 | -48 | -47.90 | 0.058 | -55.84 |
| 0.250 | -48 | -48 | -48.2 | -48.07 | 0.067 | -56.00 |
| 0.500 | -48.2 | -48.3 | -48.5 | -48.33 | 0.088 | -56.27 |
| 0.750 | -48.4 | -48.5 | -48.7 | -48.53 | 0.088 | -56.47 |
| 1.000 | -48.7 | -48.8 | -48.9 | -48.80 | 0.058 | -56.74 |
| 1.500 | -49.5 | -49.6 | -49.6 | -49.57 | 0.033 | -57.50 |
| 2.000 | -50.3 | -50.4 | -50.4 | -50.37 | 0.033 | -58.30 |

**Table A.5: Transmission data collected for different bias voltages at λ = 1550nm**

$\lambda = 1555nm$

| VRB | Pmeas1 (dBm) | Pmeas2 (dBm) | Pmeas3 (dBm) | Average | Standard Error (±) | Transmission (dB) |
|---|---|---|---|---|---|---|
| 0.000 | -46.3 | -46.6 | -46.6 | -46.50 | 0.100 | -54.60 |
| 0.250 | -46.5 | -46.5 | -46.6 | -46.53 | 0.033 | -54.63 |
| 0.500 | -46.5 | -46.5 | -46.7 | -46.57 | 0.067 | -54.67 |
| 0.750 | -46.5 | -46.6 | -46.7 | -46.60 | 0.058 | -54.70 |
| 1.000 | -46.5 | -46.6 | -46.7 | -46.60 | 0.058 | -54.70 |
| 1.500 | -46.8 | -46.9 | -47 | -46.90 | 0.058 | -55.00 |
| 2.000 | -47.2 | -47.3 | -47.5 | -47.33 | 0.088 | -55.43 |

**Table A.6: Transmission data collected for different bias voltages at λ = 1555nm**

$\lambda = 1560\text{nm}$

| VRB | Pmeas1 (dBm) | Pmeas2 (dBm) | Pmeas3 (dBm) | Average | Standard Error (±) | Transmission (dB) |
|---|---|---|---|---|---|---|
| 0.000 | -47.8 | -48 | -47.9 | -47.90 | 0.058 | -56.00 |
| 0.250 | -47.8 | -47.8 | -47.8 | -47.80 | 0.000 | -55.90 |
| 0.500 | -47.7 | -47.6 | -47.6 | -47.63 | 0.033 | -55.73 |
| 0.750 | -47.6 | -47.4 | -47.5 | -47.50 | 0.058 | -55.60 |
| 1.000 | -47.3 | -47.3 | -47.3 | -47.30 | 0.000 | -55.40 |
| 1.500 | -47.1 | -47.1 | -47.2 | -47.13 | 0.033 | -55.23 |
| 2.000 | -47.3 | -47.2 | -47.3 | -47.27 | 0.033 | -55.37 |

**Table A.7: Transmission data collected for different bias voltages at λ = 1560nm**